5 30/56

Detailed Flow-Field Measurements Over a 75° Swept Delta Wing

Scott O. Kjelgaard
and William L. Sellers III

NASA

Detailed Flow-Field Measurements Over a 75° Swept Delta Wing

Scott O. Kjelgaard
and William L. Sellers III
Langley Research Center
Hampton, Virginia

ORIGINAL CONTAINS
COLOR ILLUSTRATIONS

Summary

Results from an experimental investigation documenting the flow field over a 75° swept delta wing at an angle of attack of 20.5° are presented. Results obtained in the investigation include surface flow visualization, off-body flow visualization, and detailed flow-field surveys for various Reynolds numbers. Flow-field surveys at Reynolds numbers of 0.5×10^6, 1.0×10^6, and 1.5×10^6 based on the root chord were conducted with both a pitot pressure probe and a five-hole pressure probe, and three-component laser velocimeter surveys were conducted at a Reynolds number of 1.0×10^6. The pitot pressure surveys were obtained at five chordwise stations, the five-hole probe surveys were obtained at three chordwise stations, and the laser velocimeter surveys were obtained at one station.

The results confirm the classical roll up of the flow into a pair of primary vortices over the delta wing. The velocity measurements indicate that Reynolds number has little effect on the global structure of the flow field for the test Reynolds number range. Measurements of the nondimensionalized axial velocity in the core of the vortex indicate a jet-like flow with values greater than twice free stream. Comparisons between velocity measurements from the five-hole pressure probe and the laser velocimeter indicate that the pressure probe does a reasonable job of measuring the flow-field quantities when the velocity gradients in the flow field are low.

Introduction

Computational methods are progressing rapidly toward the prediction of the three-dimensional flow field about complex geometries at high angles of attack. These methods solve either the Euler or Navier-Stokes equations, and typically, some assumptions about the structure of the flow field are made to make the solution more tractable. These computational methods require a large number of points to adequately model the flow field, and they produce large amounts of information. To validate these methods, detailed experimental flow-field measurements are required. To date, few sets of experimental data exist which are of sufficient detail and completeness to allow a definitive validation of current computational methods.

This paper describes an experimental effort at the Langley Research Center to document the flow field over a 75° swept delta wing at an angle of attack of 20.5°. The data obtained include surface flow visualization at Reynolds numbers based on the root chord ranging from 0.5×10^6 to 2.0×10^6 in increments of 0.25×10^6; pitot pressure surveys at five chordwise

stations at Reynolds numbers of 0.5×10^6, 1.0×10^6, and 1.5×10^6; five-hole pressure probe surveys at three chordwise stations at Reynolds numbers of 0.5×10^6, 1.0×10^6, and 1.5×10^6; and three-component laser velocimeter surveys at one chordwise station at a Reynolds number of 1.0×10^6. Reynolds number variation was accomplished by changing the tunnel speed, which corresponds to a Mach number range of 0.04 to 0.11. All data obtained during this investigation are available upon request from NASA Langley Research Center, Experimental Methods Branch, M.S. 170, Hampton, VA 23665-5225. Supersonic data were previously obtained with this same model in the Langley Unitary Plan Wind Tunnel by Miller and Wood (ref. 1) and compared with computational results in reference 2. A comparison of the results from the present investigation with the results from the computational method described in reference 2 is presented in reference 3 for a Reynolds number of 0.5×10^6.

Symbols

b	local span of model, in.
C_p	static pressure coefficient, $\dfrac{p_s - p_{s,\infty}}{q}$
$C_{p,t}$	pitot pressure coefficient, $\dfrac{p_t - p_{t,\infty}}{q}$
D_p	particle diameter, ft
l	centerline length of 75° delta wing model (22.392 in.)
p_s	static pressure, lb/ft^2
p_t	pitot pressure, lb/ft^2
q	dynamic pressure, $\frac{1}{2}\rho U_\infty^2$, lb/ft^2
R	Reynolds number, $U_\infty l/\nu$
r	vortex core radius
St	Stokes number, $\frac{1}{18}\dfrac{\rho_p}{\rho}\dfrac{U_s D_p}{\nu}\dfrac{D_p}{r}$
U_s	swirl velocity near vortex core, ft/sec
U_∞	free-stream velocity, ft/sec
u, v, w	velocity components in body axis system, ft/sec
$\tilde{u}, \tilde{v}, \tilde{w}$	velocity components in tunnel axis system, ft/sec
u'	root mean square (rms) of fluctuating component of $\tilde{u}$ velocity, ft/sec
$\mathbf{V}$	local flow velocity vector, ft/sec
x, y, z	distance from coordinate origin in body axis system, in.

$\tilde{x}, \tilde{y}, \tilde{z}$ distance from coordinate origin in tunnel axis system, in.

α pitch angle of flow with respect to probe axis, deg

β yaw angle of flow with respect to probe axis, deg

Γ circulation, ft^2/sec

η nondimensionalized semispan location, $\frac{y}{b/2}$

θ total flow angle with respect to X-axis, $\sin^{-1}\left(\frac{\sqrt{v^2+w^2}}{\sqrt{u^2+v^2+w^2}}\right)$

ν kinematic viscosity, ft^2/sec

ρ density, $slugs/ft^3$

ω nondimensionalized vorticity, $\frac{l}{U_\infty}\left(\frac{\partial v}{\partial z}-\frac{\partial w}{\partial y}\right)$

Subscripts:

meas   measured

p particle

t transition

∞ free-stream conditions

Test Facility and Data Acquisition System

The 75° swept delta wing was tested in the Langley Basic Aerodynamics Research Tunnel (BART). The BART is an open-return wind tunnel with a test section 28 in. high, 40 in. wide, and 10 ft long. The maximum test section velocity is 220 ft/sec which yields a Reynolds number per foot of 1.4×10^6. The airflow entering the test section is conditioned by a honeycomb, four antiturbulence screens, and a contraction ratio of 11:1. A photograph of the facility is shown in figure 1.

The effect of free-stream turbulence intensity on vortex structures is not understood at this time; therefore, the variation of the longitudinal component of turbulence intensity as measured with a normal wire with test-section q is presented in figure 2. The figure indicates that the turbulence intensity ranges from 0.05 to 0.08 percent at test-section q of 10 and 45 lb/ft^2, respectively. The fluctuating voltage from the normal wire was conditioned with a high-pass filter of 1 Hz and a low-pass filter of 10 kHz.

Model Description

The model used in this investigation was a 75° swept delta wing. A sketch of the model is presented in figure 3. The model has a centerline length of 22.392 in. and a span of 12 in. The upper surface of the delta wing was flat. The leading edge of the delta wing is sharp (0.005 in. radius) with a chamfer of 10° normal to the leading edge. The model was attached to the model support system at $x/l = 0.64$ on the lower surface. Figure 4 shows the delta wing mounted in the test section.

Experimental Techniques

Flow Visualization

Surface flow visualizations were conducted at Reynolds numbers ranging from 0.5×10^6 to 2.0×10^6 in increments of 0.25×10^6. The upper surface of the model was covered with a black vinyl adhesive-backed paper. A mixture of titanium dioxide (TiO_2) suspended in kerosene, with a small amount of oleic acid added as an anticoagulant, was painted on the vinyl paper with a brush. The airspeed in the test section was brought to test conditions, and after the kerosene had evaporated, the TiO_2 was left deposited on the surface. The vinyl paper was then carefully lifted off the surface, placed on poster board, and photographed for a permanent record.

Laser light sheet flow visualization was used to see if the vortices shed by the model were burst and to determine if the probes used in this investigation had any visible effect on the vortices. The laser light sheet was produced with a 5-W argon ion laser as the light source with a twin-mirrored galvanometer light sheet generator as described in reference 4. The smoke was produced by vaporizing propylene glycol at a temperature of 380°F and introduced into the tunnel circuit ahead of the honeycomb. Figure 5 shows a typical laser light sheet photograph and illustrates the capability of the system to produce simultaneous multiple light sheets.

Pitot Pressure Surveys

Pitot pressure surveys were conducted at $x/l = 0.3, 0.5, 0.7, 0.9,$ and 1.1 in planes normal to the free-stream direction for Reynolds numbers of 0.5×10^6, 1.0×10^6, and 1.5×10^6. The probe used was a boundary-layer probe approximately 0.024 in. wide by 0.013 in. high with a wall thickness of 0.005 in. A sketch of the pitot pressure probe is presented in figure 6. The pitot pressure probe was always aligned parallel to the free-stream direction.

Whenever a probe is introduced into a complex flow field, the effect of the probe on the flow field

must be considered as well as the measurement characteristics of the probe. The pitot pressure probe used in this investigation was chosen because its extremely small size enabled measurements to be made with high spatial resolution in the flow field. It was recognized at the outset of the investigation that the probe would not be capable of measuring the true total pressure since it is always aligned in the free-stream direction and not in the direction of the local flow. Figure 7 presents the pitot pressure measured by the probe as a function of the yaw angle. The figure shows that the probe has a plateau region of only ±7° and its response rolls off sharply outside this range. The same response was measured for both pitch and yaw at multiple free-stream dynamic pressures.

A computer-controlled probe-positioning system with a 0.0005-in. resolution was used to traverse the probe through the flow field above the delta wing. At the beginning of each survey and after the airspeed was brought to test condition, the model surface was located through the use of an electrical probe fouling circuit. This was done to lessen the effect of the probe and model deflections under aerodynamic loading. Once the model surface was located, the flow-field survey was conducted. A typical flow-field survey consisted of a grid of approximately 91 points horizontally by 31 points vertically ($\approx$2800 data points per survey location) with a spacing between points equal to 1.67 percent of the local span. The data acquisition software also allowed the researcher to specify an embedded survey grid in the survey just acquired. In this investigation, the embedded grid option was used for a more detailed survey of the secondary vortex. The embedded grids typically contained 1700 data points with a grid spacing equal to 0.35 percent of the local span.

Pressure data were acquired with an electronic-scanning pressure system with 5-psid transducers deranged to 1 psid. The accuracy of these transducers is ±0.002 psi. This accuracy is a function of temperature (±0.0005 psi/°F); therefore, the data acquisition system continuously monitored the temperature where the transducers were located and automatically performed a calibration when the temperature changed more than 2°F. After stepping to each measurement location and pausing 0.5 sec to allow for pressure stabilization, the mean pressure was determined by averaging 255 samples acquired over a time interval of 1 sec. The pitot pressure was measured by referencing the pressure transducers to the total pressure downstream of the last antiturbulence screen. The pitot pressure was nondimensionalized by the free-stream dynamic pressure to obtain the pitot pressure coefficient $C_{p,t}$.

Five-Hole Probe Surveys

Five-hole probe surveys were conducted to measure flow angularity and velocity above the delta wing. These surveys were obtained at $x/l = 0.7, 0.9$, and 1.1 in planes normal to the free-stream direction for Reynolds numbers of 0.5×10^6, 1.0×10^6, and 1.5×10^6.

The probe used in this investigation was a hemispherically tipped, 0.125-in-diameter five-hole pressure probe. A sketch of the probe is presented in figure 8. Equations defining the potential flow over a sphere can relate the pressure difference between the ports to the flow velocity. These equations can be generalized to allow for viscous effects, and constants for the equations can be determined from calibration data. The derivation of the calibration equations and the method of acquiring the calibration data are described in reference 5. The errors in α, β, and q deduced from the five-hole probe calibration data are presented in figure 9. The five-hole probe was always aligned in the free-stream direction and used the same probe positioning system and pressure measurement technique described previously. A typical flow-field survey consisted of a grid similar to that of the measurements of $C_{p,t}$ ($\approx$3300 data points per survey location). The embedded survey grid option was not used because the large size of the probe relative to the secondary vortex would not yield good resolution of the vortex.

Laser Velocimeter Surveys

The BART is equipped with a dedicated three-component laser velocimeter (LV) system to enable the nonintrusive measurement of flow fields. The LV is capable of obtaining accurate velocity measurements in flow fields with reverse flows, large shear gradients, and velocity fluctuations. For this investigation, an LV survey was obtained at the longitudinal station $x/l = 0.9$ at a Reynolds number of 1.0×10^6 for comparison with the five-hole pressure probe results.

The BART LV system (fig. 10) is a three-color, orthogonal, crossed-fringe configuration with the receive optics mounted 90° off-axis. The 514.5-, 496.5-, and 476.5-nm wavelengths are used to acquire the lateral ($\tilde{v}$), streamwise ($\tilde{u}$), and vertical ($\tilde{w}$) velocity components, respectively. Bragg cells are used to provide directional measurement capability in all three velocity components. The sample volume is spherical in shape and has been calculated to be approximately 150 μm in diameter. The optics and laser move as a unit on a traversing system that provides 1 m of travel with 10-μm resolution in all three axes. Additional information detailing the LV is presented in reference 6.

The flow field was seeded with 0.8-μm polystyrene latex microspheres. The seed particles were suspended in a mixture of alcohol and water and were injected into the flow upstream of the honeycomb with an atomizing spray nozzle. Typically 500 to 4096 velocity samples were obtained at each measurement location in the flow field. The actual number of samples depended on the particular location in the flow field and the particle seeding rate.

The LV measures the velocity of the seed particles; therefore, it is important that the particle track the streamlines accurately. The ability of the particle to follow the streamline is directly related to the size of the particle. Theoretical predictions of particle trajectories in various flows were reported in references 7 through 10. Dring and Suo (ref. 7) concluded that the particle trajectory in a free vortex swirling flow is governed primarily by the Stokes number, St, and when St is less than 0.01, the particle will follow the circular streamlines of the free vortex.

The 0.8-μm particles used during this test have a density ρ_p of 2.03727 slugs/ft^3. The Stokes number for the particles, based on the radius and the swirl velocity at the edge of the vortex core, is 0.007. The numerical procedure described by Dring and Suo (ref. 7) was used to predict the particle trajectories for the vortices that were measured during this investigation. The predictions show that the particles used during this test follow the streamlines of the vortex with an accuracy of about 1 percent.

Results and Discussion

Flow Visualization

A brief description of the flow over a swept delta wing will aid in the subsequent discussion of the results. At moderate to high angles of attack, the airflow separates at the sharp leading edge of a swept delta wing. The separated shear layer rolls up into two primary vortices as sketched in figure 11 (from ref. 11). As the airflow rolls up and over the primary vortices, it impinges on the surface along the primary attachment line and then flows outward. The influence of these two vortices on the wing upper surface produces suction pressures near the delta wing leading edge (fig. 11(a)). Because of the steep adverse pressure gradients induced outboard of the primary vortex, the boundary layer separates and a secondary vortex may form in the region between the boundary-layer separation and the leading edge. These smaller secondary vortices induce additional velocities on the surface and cause further modification of the wing pressure distribution. Depending on Reynolds number, additional tertiary separations may also occur.

The secondary separation lines appear as rays emanating from the apex of the delta wing as shown in figure 11(b). When the boundary-layer transition from laminar to turbulent occurs, the position of the secondary separation shifts outward toward the leading edge as described by Hummel in reference 11. Vortex bursting will also cause a shift in the secondary separation line. In fact, Lambourne and Bryer (ref. 12) described a situation in which the vortex bursting over the surface of the wing caused an outward shift or bending in the secondary separation line because of a reduction in the adverse pressure gradient and an increase in turbulence. This was not the case in this investigation, since the laser light sheet flow visualization, as in figure 5, confirmed that the vortices did not burst over the entire Reynolds number range of the test.

The region where the boundary-layer transition from laminar to turbulent occurs is important for validating computational methods, especially Reynolds-averaged Navier-Stokes codes which use turbulence models. Therefore, boundary-layer transition was not fixed on either the upper or lower wing surfaces. Surface flow visualizations using titanium dioxide and kerosene were used to characterize the state of the boundary layer for Reynolds numbers between 0.5×10^6 and 2.0×10^6. The complete set of surface flow visualizations are presented in figure 12. The surface flow visualizations were digitized to obtain the location of the secondary separation lines and these data are presented in figure 13. The figure shows the position of the secondary separation lines for the Reynolds numbers used in the investigation. The Reynolds number where transition begins is defined as

$$R_t = \frac{x_t U_\infty}{\nu}$$

where x_t is the streamwise distance from the apex to where transition begins. The transition Reynolds number ranged from 0.8×10^6 to 0.9×10^6, which agrees well with the results of Hummel presented in reference 11. The figure shows that the transition of the boundary layer occurs at the trailing edge of the wing at a Reynolds number of approximately 1.0×10^6 and moves forward to $x/l \approx 0.4$ at a Reynolds number of 2.0×10^6.

Pitot Pressure Coefficient $C_{p,t}$

As stated previously, whenever a probe is introduced into a complex flow field, the effect of the probe on the flow field must be considered as well as the measurement characteristics of the probe. Flow visualization has confirmed that the presence of the probe did not cause premature bursting of the vortex or any visually perceptible disturbance to either

the primary or secondary vortices for the flow conditions of this investigation. The pitot pressure probe used for these flow-field surveys was chosen because its small size enabled measurements to be made with high spatial resolution. It was recognized at the outset of the investigation that the probe would not be capable of measuring the true total pressure since it is always aligned in the free-stream direction and not in the direction of the local flow. Since the sensitivity of the pitot pressure probe is known, the measured data can be compared with computational results which predict pressure and velocity at all points in the flow field. Velocity and static pressure field data from computational methods can be used to compute a reduced total pressure coefficient, based on bringing only the component of the local velocity vector aligned with the free stream to rest. The pitot pressure data presented in this paper are uncorrected for effects due to the probe.

Figure 14 presents a typical contour plot of the pitot pressure coefficient. The results indicate a high gradient in $C_{p,t}$ just outboard of the primary vortex core. It also shows two interesting regions where $C_{p,t}$ measured in the flow field is very nearly equal to $C_{p,t}$ measured in the free stream. The first region appears as a hole between the free shear layer and the cores of the primary vortices. The second is a roughly triangular region at the centerline of the wing near the surface. These features were interesting because they were not apparent in the smoke patterns of the laser light sheet or in previous investigations on a similar geometry (ref. 11). Comparisons of these data with the reduced total pressure coefficient data obtained from the CFL3D Navier-Stokes code (fig. 15) show that these two regions are caused by the inability of the probe to measure the true total pressure coefficient. A more complete comparison of these data are presented in reference 13.

Figure 16 presents color contours of the pitot pressure coefficient data acquired over the 75° swept delta wing at x/l = 0.3, 0.5, 0.7, 0.9, and 1.1 superimposed on the TiO$_2$ surface flow visualization for Reynolds numbers of 0.5×10^6, 1.0×10^6, and 1.5×10^6.

Figure 17 presents typical $C_{p,t}$ data acquired during an embedded survey of the secondary vortex ($-y$) for x/l = 0.9, $R = 0.5 \times 10^6$, 1.0×10^6, and 1.5×10^6. The figure shows that the transition of the boundary layer from laminar to turbulent changes the structure of the secondary vortex. For a Reynolds number of 0.5×10^6 at x/l = 0.9, the laminar boundary-layer separation occurs at $\eta \approx 0.6$. Figure 17(a) shows a large value of $C_{p,t}$ (≈ 1.5) in the region just after boundary-layer separation. For a Reynolds number of 1.5×10^6, the turbulent boundary-layer separation

occurs at $\eta \approx 0.8$. Figure 17(c) does not show the large values of $C_{p,t}$, and the spatial extent of the secondary vortex is significantly reduced from that of the 0.5×10^6 case.

Velocity Surveys

Velocity surveys were obtained for x/l = 0.7, 0.9, and 1.1 for Reynolds numbers of 0.5×10^6, 1.0×10^6, and 1.5×10^6. A typical cross-flow vector survey is shown in figure 18. In this case, the longitudinal station was x/l = 0.9 and R was 1.0×10^6. Figures 19, 20, and 21 present velocity contours for all three components for Reynolds numbers of 0.5×10^6, 1.0×10^6, and 1.5×10^6, respectively. These figures indicate that Reynolds number has little influence over the primary vortex structure. The jet-like flow in the vortex core has the same maximum longitudinal component of velocity u/U_∞ for all Reynolds numbers for each respective constant x station.

Once again, one must consider the effect that the probe has on the flow field as well as the ability of the probe to measure the flow angle and velocity in a nonuniform velocity field. As stated before, laser light sheet flow visualization showed that the probe had no visible effect on the position or structure of the primary or secondary vortex cores. Figure 9 shows the measurement errors for the five-hole probe in a uniform flow field. However, the flow field over the 75° wing has large gradients in the lateral and vertical components of velocity as shown in figure 22 (≈ 6000 ft/sec/ft). To assess the measurement errors of the five-hole probe in this high gradient flow field, a velocity survey was obtained with a three-component LV at the same points above the delta wing as the five-hole probe. Figure 23 presents the differences between the LV and the five-hole probe results for the u, v, and w components of velocity. In the core of the vortex, the five-hole probe has errors in u, v, and w of 25, 17, and 35 percent of the total velocity, respectively. The errors were calculated with the assumption that the LV measurements were the reference. The equation used to calculate the u component error is as follows:

$$u_{\text{error}} = 100 \times \frac{(u_{\text{LV}} - u_{\text{5-hole}})}{\sqrt{u_{\text{LV}}^2 + v_{\text{LV}}^2 + w_{\text{LV}}^2}}$$

The figure shows that, for regions of low velocity gradients (< 800 ft/sec/ft), the five-hole probe does a reasonable job of measuring the flow-field quantities (probe error < 5 percent). The five-hole probe flow-field survey data presented in this paper are uncorrected for effects due to the probe.

Vorticity

The vorticity ω calculated from a velocity field can vary significantly due to differences in grid size and density. There are two commonly used techniques to calculate vorticity. The first method uses a finite difference algorithm to approximate the gradient terms $\frac{\partial v}{\partial z}$ and $\frac{\partial w}{\partial y}$ in the calculation of vorticity. The second method is based on Green's theorem and calculates the circulation, $\Gamma = \oint \mathbf{V}\, d\ell$, about a bounding path (typically a rectangle) and divides Γ by the enclosed area to compute the vorticity. The vorticity data presented in this paper were calculated by the second method.

The velocity data obtained with the five-hole probe were used to calculate the streamwise vorticity in the flow field above the delta wing. Streamwise vorticity contours are presented in figure 24 for Reynolds numbers of 0.5×10^6, 1.0×10^6, and 1.5×10^6. The data show that the nondimensionalized vorticity level in the primary vortex for a given x station does not change significantly over the Reynolds number range.

The maximum value of vorticity in a velocity field is very sensitive to grid size, placement, and density and, therefore, is not a good parameter for a detailed comparison. The vorticity data presented by Carcaillet et al. in reference 14 provide a good example. The data were generated by a 75° swept delta wing at Reynolds numbers bracketing the present experiment. Even though very similar finite difference techniques were used and the survey grids were approximately the same, the data in reference 14 show almost twice the maximum vorticity level in the core when compared with those measured in this experiment (fig. 25). Figure 26 presents the vorticity calculated from the experiment and the vorticity calculated from results of the CFL3D Navier-Stokes code (ref. 15). Good agreement in the vorticity is found between the experiment and computation.

Summary of Results

An experimental investigation documenting the flow field over a 75° swept delta wing at an angle of attack of 20.5° was made. Results obtained in the investigation include surface flow visualization, off-body flow visualization, and detailed flow-field surveys for various Reynolds numbers. Flow-field surveys at Reynolds numbers of 0.5×10^6, 1.0×10^6, and 1.5×10^6 were conducted with a pitot pressure probe at five chordwise stations and with a five-hole pressure probe at three chordwise stations. Three-component laser velocimeter surveys were made at a Reynolds number of 1.0×10^6 at one station. The results are as follows:

1. Surface flow visualization was obtained at Reynolds numbers ranging from 0.5×10^6 to 2.0×10^6 in increments of 0.25×10^6. This surface flow visualization data confirmed the previously reported transition Reynolds number of 0.8×10^6.

2. Flow visualization has confirmed that the presence of the probe did not cause premature bursting of the vortex or any visually perceptible disturbance to either the primary or secondary vortices for the flow conditions of this investigation.

3. The nondimensionalized velocities indicate that Reynolds number has little effect on the global structure of the flow field for the test Reynolds number range.

4. Results from the five-hole probe indicate a jet-like flow in the vortex core with a nondimensionalized longitudinal velocity greater than 2.0.

5. The vortical flow field contains gradients on the order of 6000 ft/sec/ft.

6. Comparisons between the velocities measured by the five-hole probe and those measured by the three-component laser velocimeter indicate that the five-hole probe does a reasonable job of measuring flow-field quantities when the gradients in the flow field are less than 800 ft/sec/ft. However, errors as high as 35 percent are seen in the region of the vortex core.

7. The vorticity calculated from the velocity data agrees well with those calculated from results of a Navier-Stokes code.

NASA Langley Research Center
Hampton, VA 23665-5225
August 6, 1990

References

1. Miller, David S.; and Wood, Richard M.: *Lee-Side Flow Over Delta Wings at Supersonic Speeds.* NASA TP-2430, 1985.

2. Thomas, J. L.; Taylor, S. L.; and Anderson, W. K.: Navier-Stokes Computations of Vortical Flows Over Low Aspect Ratio Wings. AIAA-87-0207, Jan. 1987.

3. Taylor, Sherrie L.; Kjelgaard, Scott O.; Weston, Robert P.; Thomas, James L.; and Sellers, William L., III: Experimental and Computational Study of the Subsonic Flow About a 75° Swept Delta Wing. AIAA-87-2425, Aug. 1987.

4. Rhodes, David B.; Franke, John M.; Jones, Stephen B.; and Leighty, Bradley D.: *A Twin-Mirrored Galvanometer Laser Light Sheet Generator.* NASA TM-100587, 1988.

5. Kjelgaard, Scott O.: *Theoretical Derivation and Calibration Technique of a Hemispherical-Tipped Five-Hole Probe.* NASA TM-4047, 1988.

6. Meyers, James F.; and Hepner, Timothy E.: Measurement of Leading Edge Vortices From a Delta Wing Using a Three Component Laser Velocimeter. *A Collection of Technical Papers—AIAA 15th Aerodynamic Testing Conference*, May 1988, pp. 223–233. (Available as AIAA-88-2024.)

7. Dring, R. P.; and Suo, M.: Particle Trajectories in Swirling Flows. *J. Energy*, vol. 2, no. 4, July–Aug. 1978, pp. 232–237.

8. Dring, R. P.; Caspar, J. R.; and Suo, M.: Particle Trajectories in Turbine Cascades. *J. Energy*, vol. 3, no. 3, May–June 1979, pp. 161–166.

9. Dring, R. P.: Sizing Criteria for Laser Anemometry Particles. *Trans. ASME, J. Fluids Eng.*, vol. 104, Mar. 1982, pp. 15–17.

10. Vorropoulos, G.; and Wendt, J. F.: Laser Velocimetry Study of Compressibility Effects on the Flow Field of a Delta Wing. *Aerodynamics of Vortical Type Flows in Three Dimensions*, AGARD-CP-342, July 1983, pp. 9-1–9-13.

11. Hummel, Ing. Dietrich: On the Vortex Formation Over a Slender Wing at Large Angles of Incidence. *High Angle of Attack Aerodynamics*, AGARD-CP-247, Jan. 1979, pp. 15-1–15-17.

12. Lambourne, N. C.; and Bryer, D. W.: *The Bursting of Leading-Edge Vortices—Some Observations and Discussion of the Phenomenon.* R. & M. No. 3282, British Aeronautical Research Council, Apr. 1961.

13. Kjelgaard, Scott O.; Sellers, William L., III; and Weston, Robert P.: Flowfield Survey Over a 75° Swept Delta Wing at an Angle of Attack of 20.5°. AIAA-86-1775, June 1986.

14. Carcaillet, R.; Manie, F.; Pagan, D.; and Solignac, J. L.: *Leading Edge Vortex Flow Over a 75 Degree-Swept Delta Wing—Experimental and Computational Results.* ONERA T.P. No. 1986-122, Sept. 1986.

15. Krist, Sherrie L.; Thomas, James L.; Sellers, William L., III; and Kjelgaard Scott O.: An Embedded Grid Formulation Applied to a Delta Wing. AIAA-90-0429, Jan. 1990.
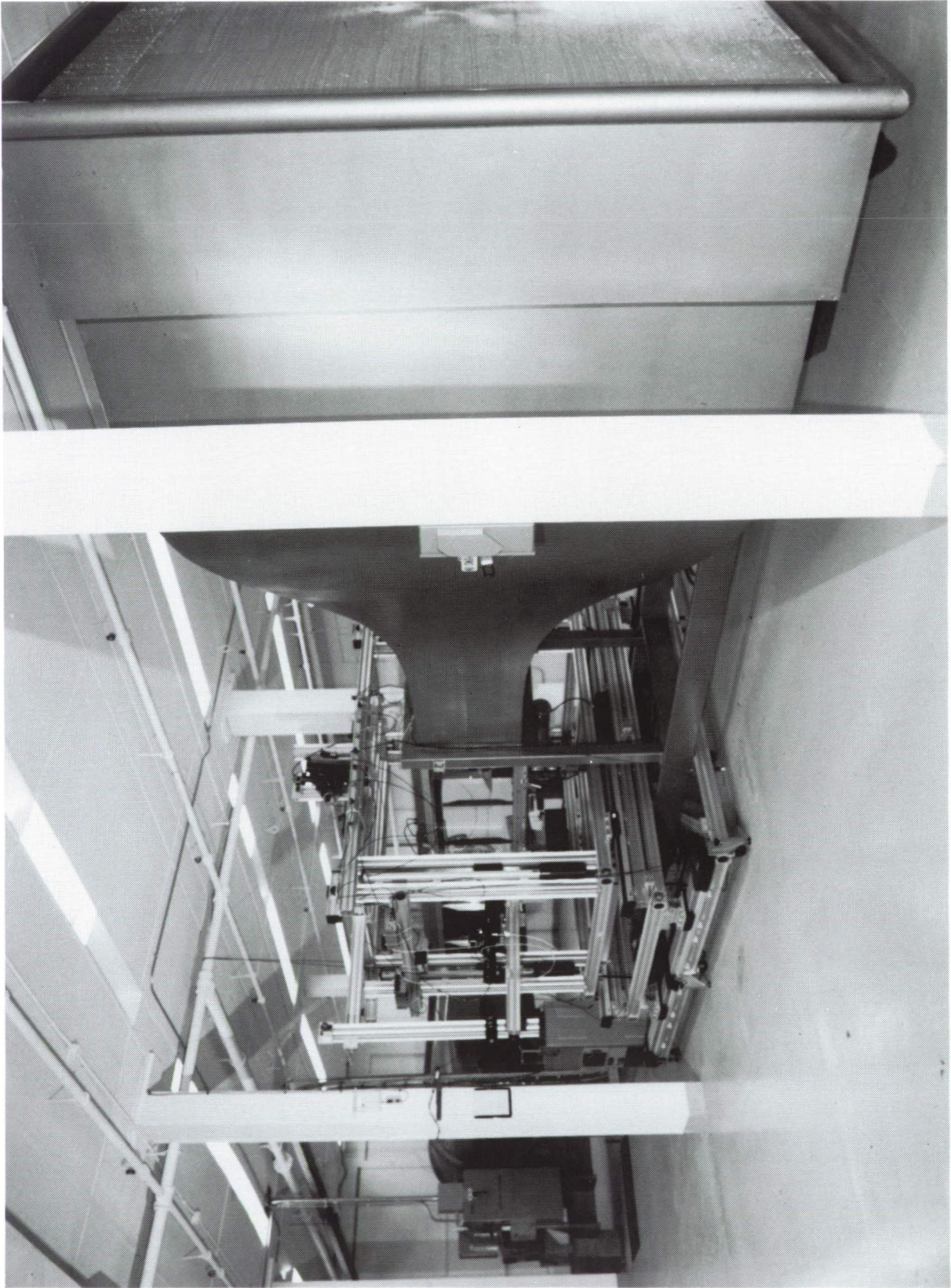
L-87-4185

Figure 1. Langley Basic Aerodynamics Research Tunnel (BART).
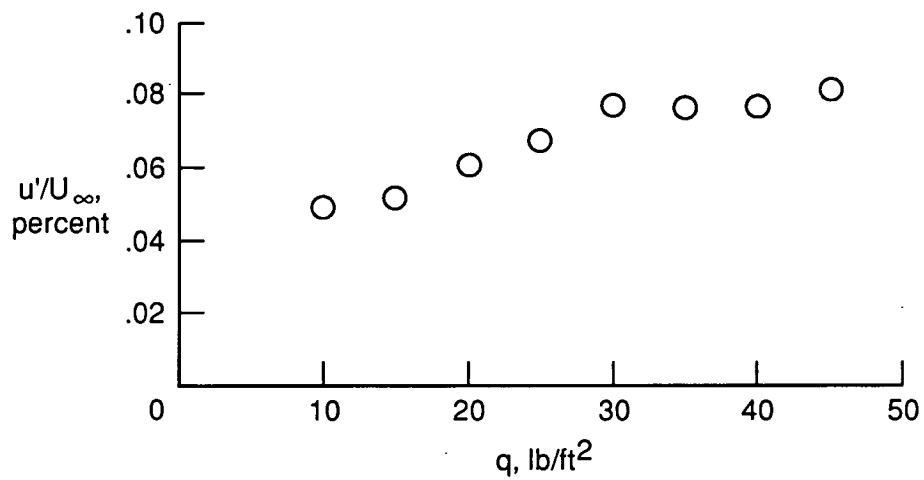
Figure 2. Variation of longitudinal component of velocity fluctuations with test-section dynamic pressure.
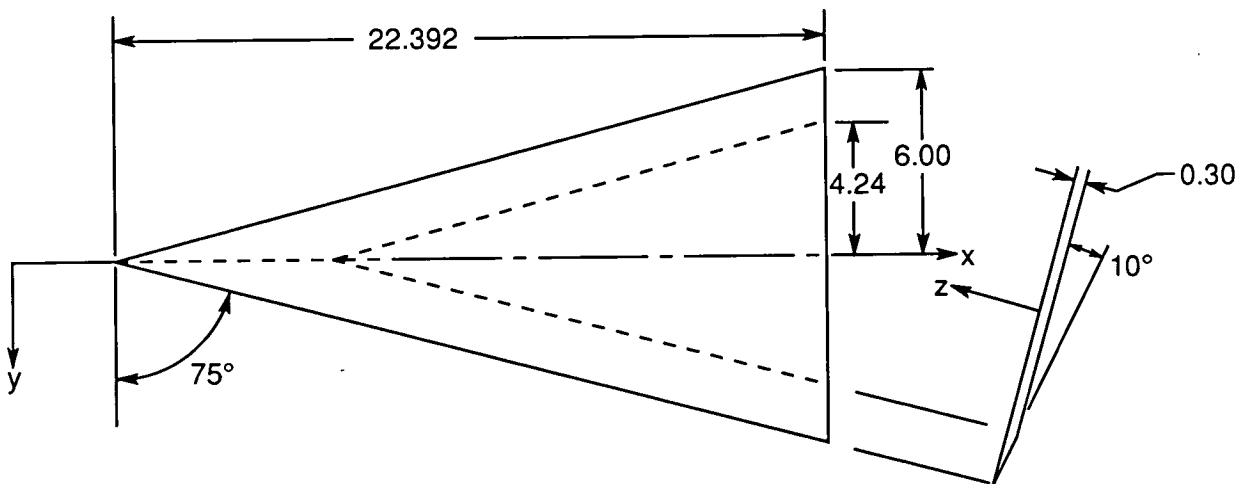
Figure 3. Sketch of 75° swept delta wing model. Linear dimensions are in inches.
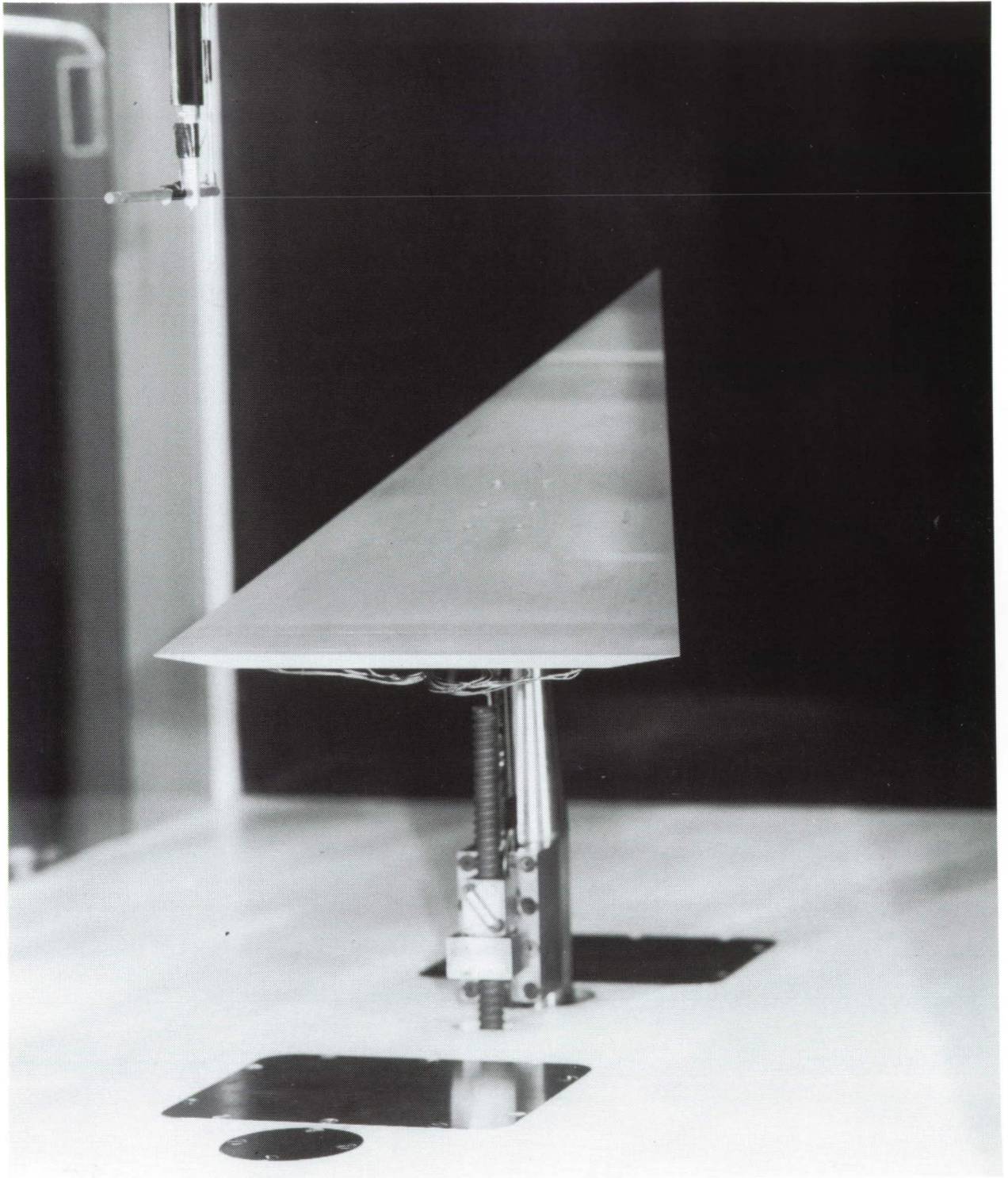
L-86-2867

Figure 4. The 75° swept delta wing in BART test section.
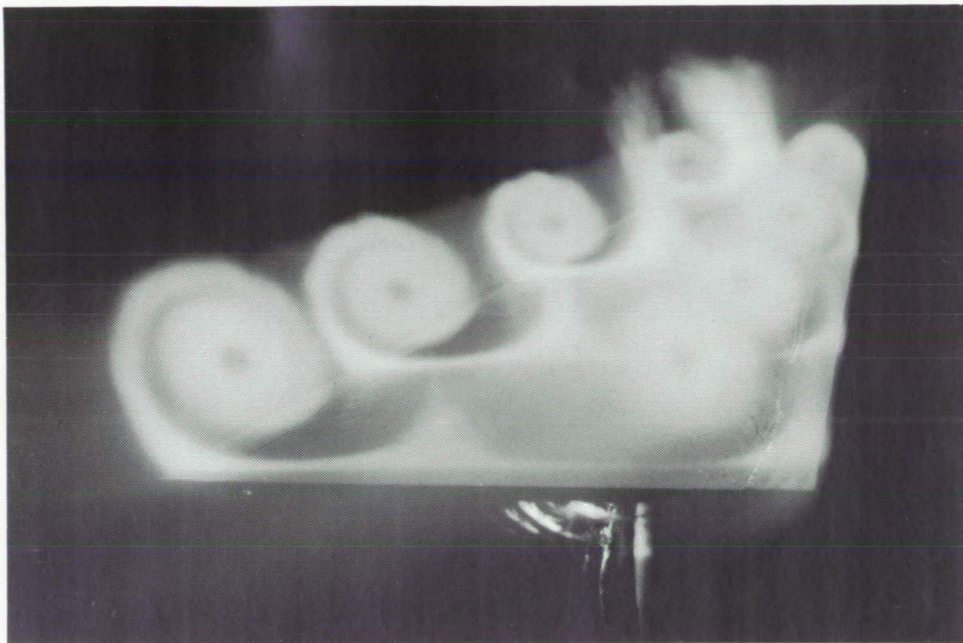
L-86-11800

Figure 5. Typical laser light sheet flow visualization. $\alpha = 20.5°$; $R = 1.0 \times 10^6$.
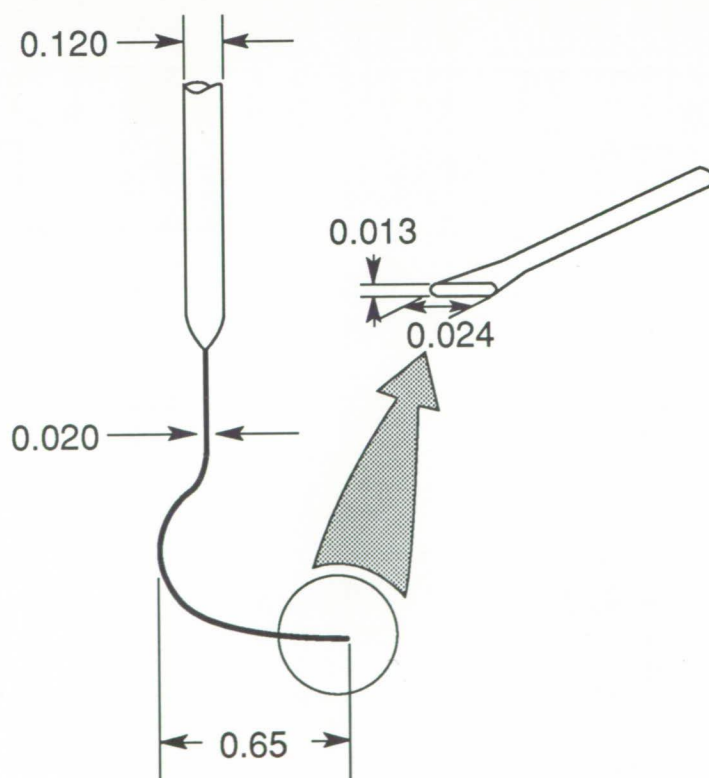
Figure 6. Sketch of pitot pressure probe used during this investigation. Dimensions are in inches.
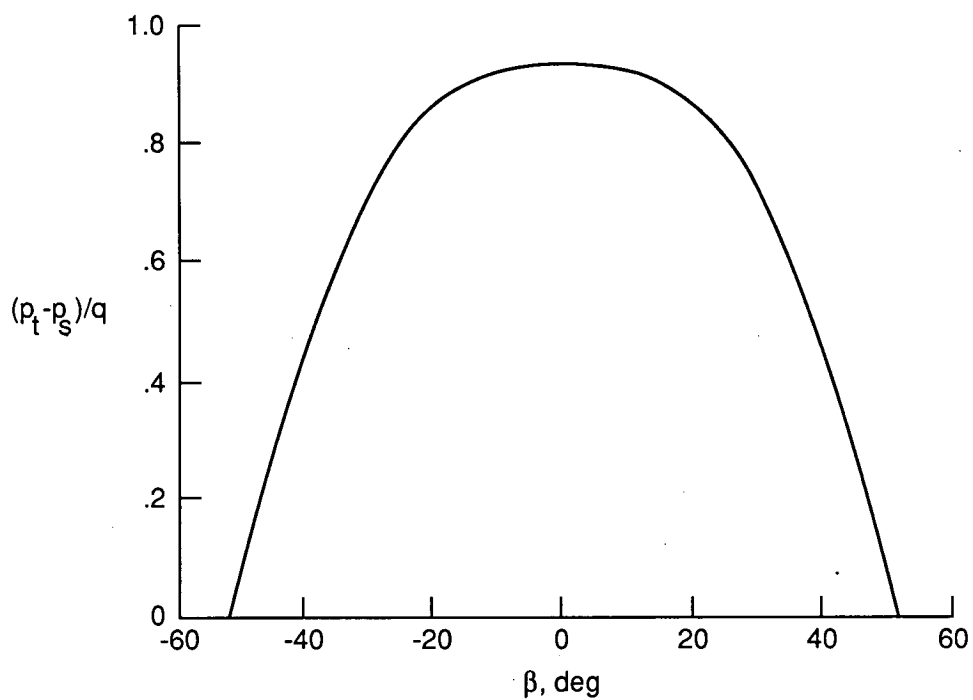
Figure 7. Sensitivity of pitot pressure probe to yaw.
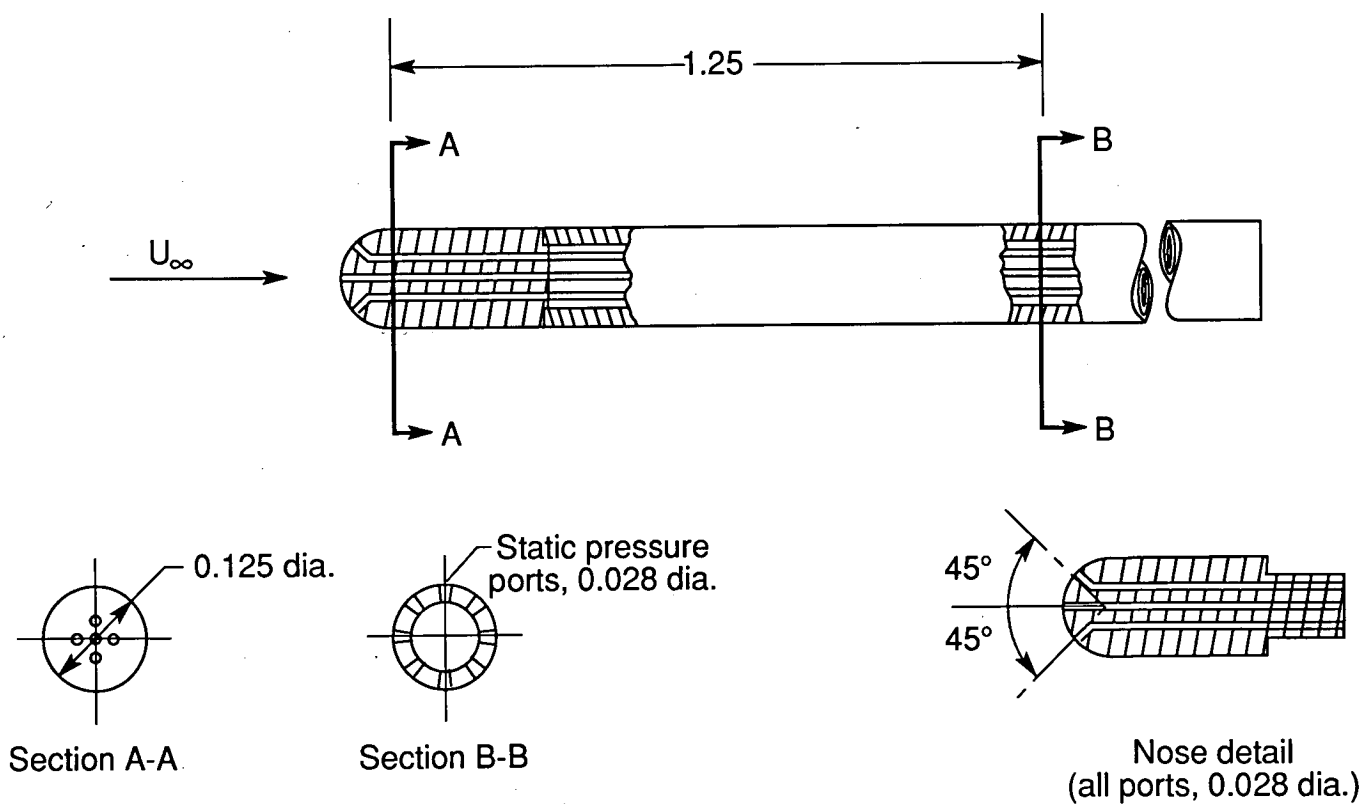
Figure 8. Sketch of five-hole pressure probe used during this investigation. Linear dimensions are in inches.
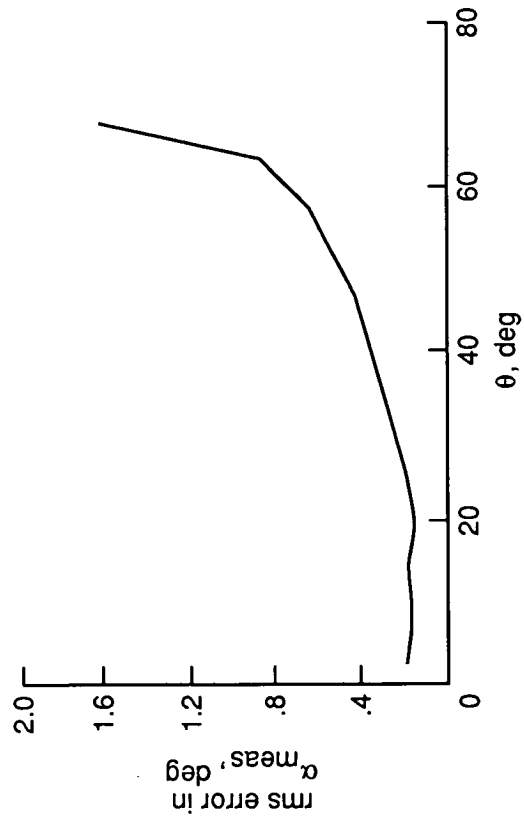
(a) rms error in α_{meas}.
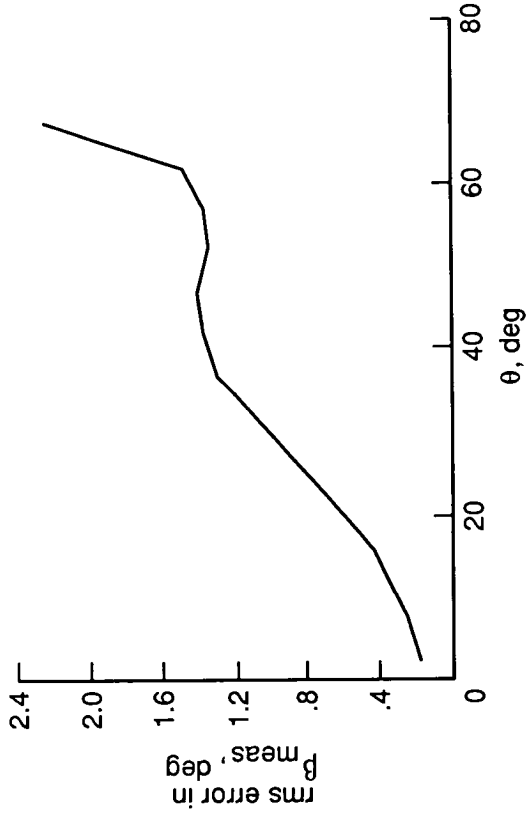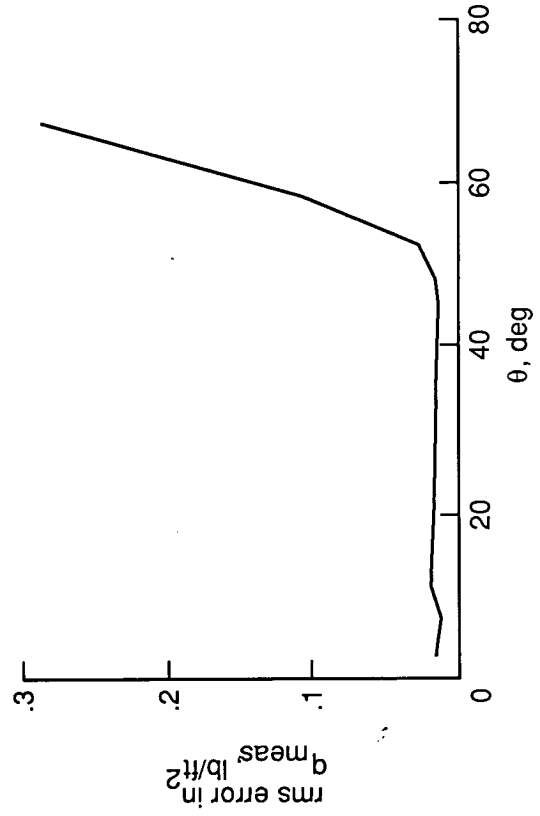
(b) rms error in β_{meas}.

(c) rms error in q_{meas}.

Figure 9. Errors in parameters measured by five-hole probe in uniform flow.

13

ũ,w̃ receive optics

5-W argon ion laser

ṽ transmit optics

ṽ receive optics

ũ,w̃ transmit optics
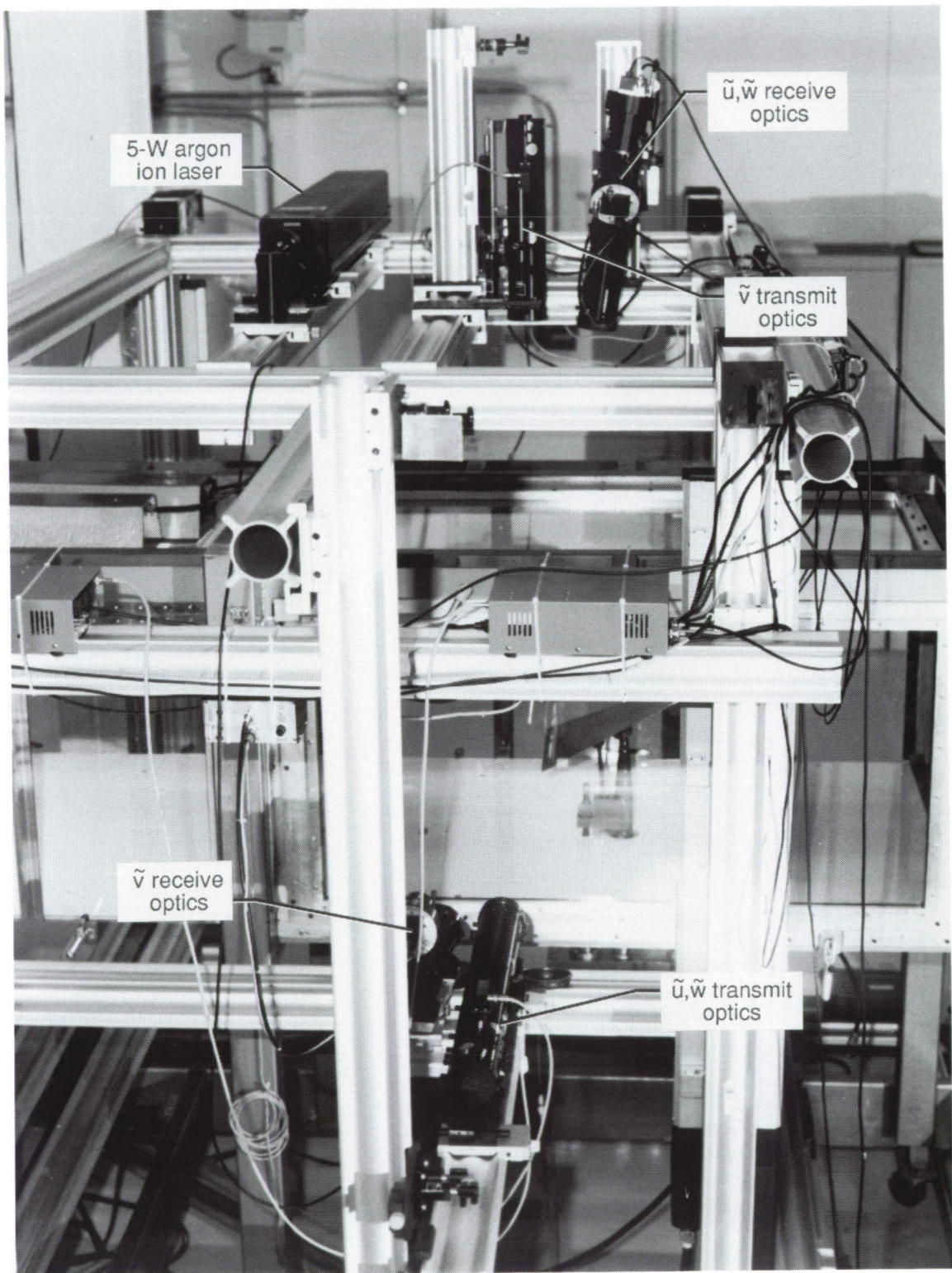
L-90-42

Figure 10. BART three-component laser velocimeter.

14
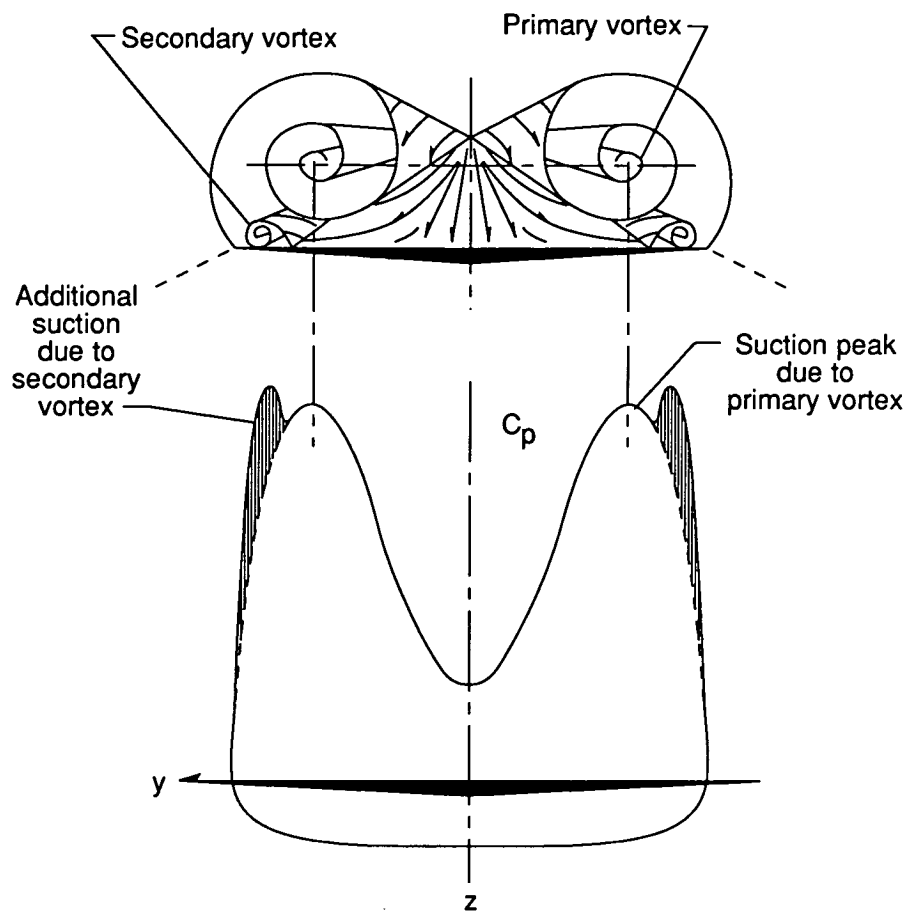
(a) Cross-flow schematic and typical surface pressure distribution.
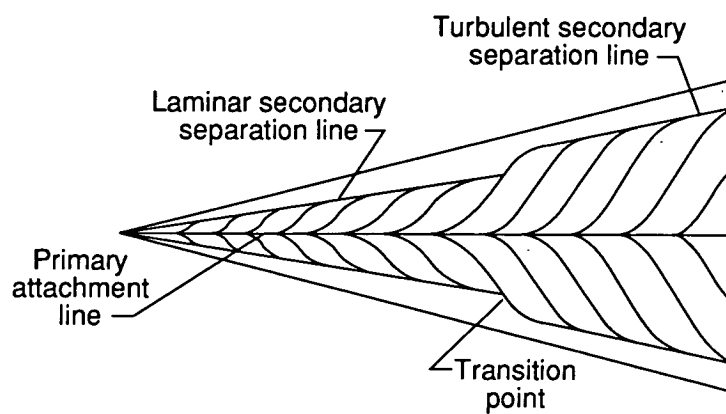
(b) Surface flow schematic.

Figure 11. Vortical flow over a slender sharp-edged delta wing. (See ref. 11.)
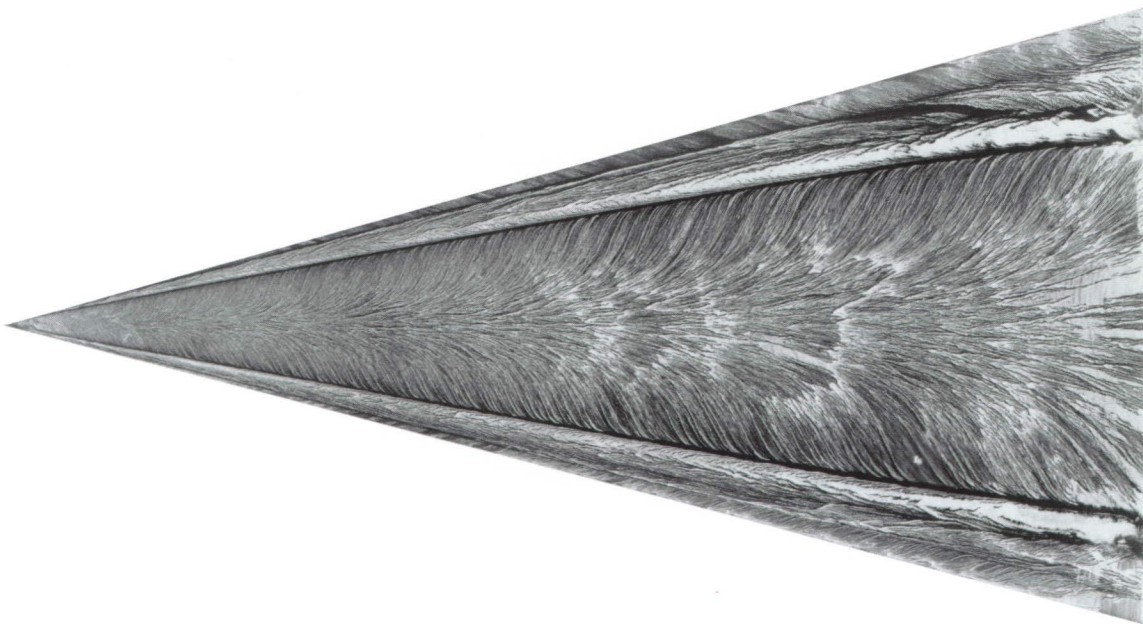
(b) $R = 0.75 \times 10^6$.

(a) $R = 0.5 \times 10^6$.

Figure 12. Surface flow visualization using TiO_2.

(d) $R = 1.25 \times 10^6$.

(c) $R = 1.0 \times 10^6$.

Figure 12. Continued.

(f) $R = 1.75 \times 10^6$.

(e) $R = 1.5 \times 10^6$.

Figure 12. Continued.

(g) $R = 2.0 \times 10^6$.

Figure 12. Concluded.

(a) $-y$.

(b) $+y$.
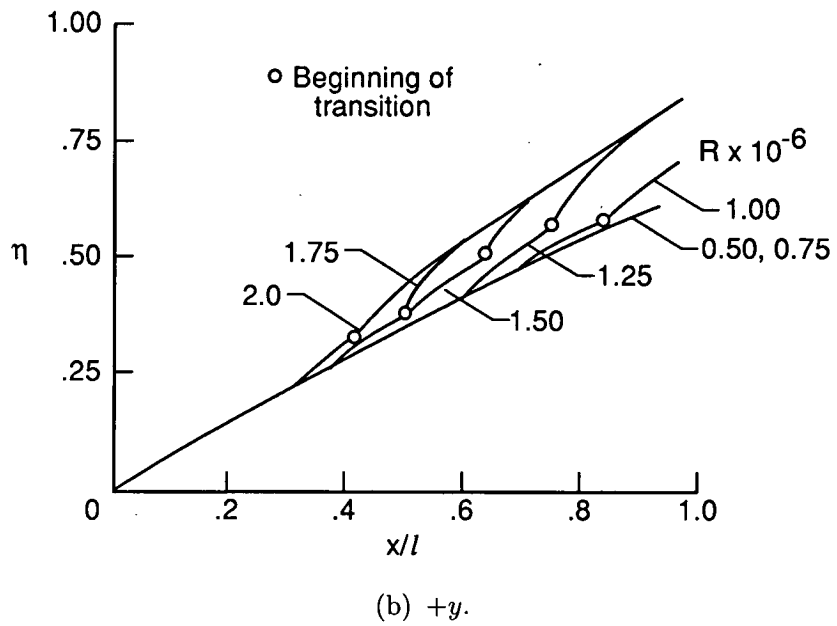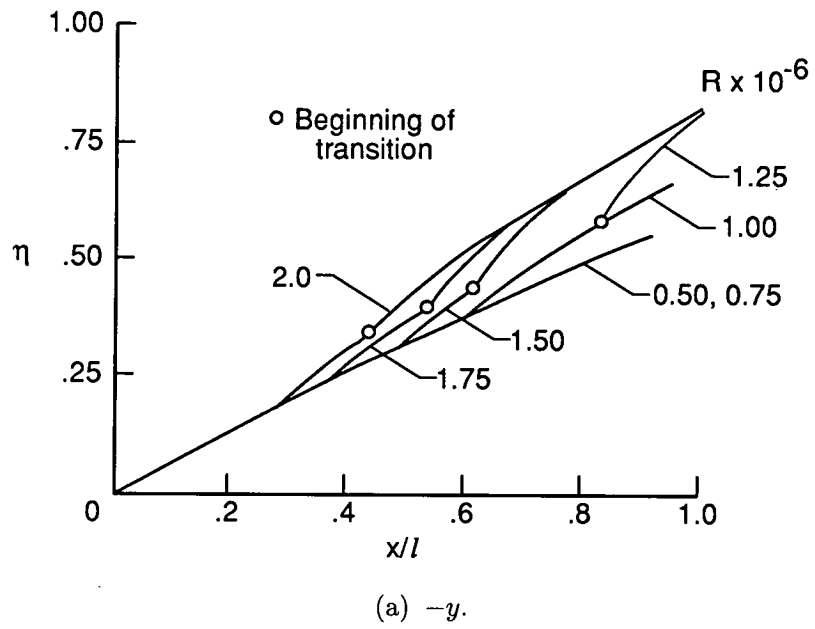
Figure 13. Secondary separation positions measured from TiO_2 surface flow visualizations.
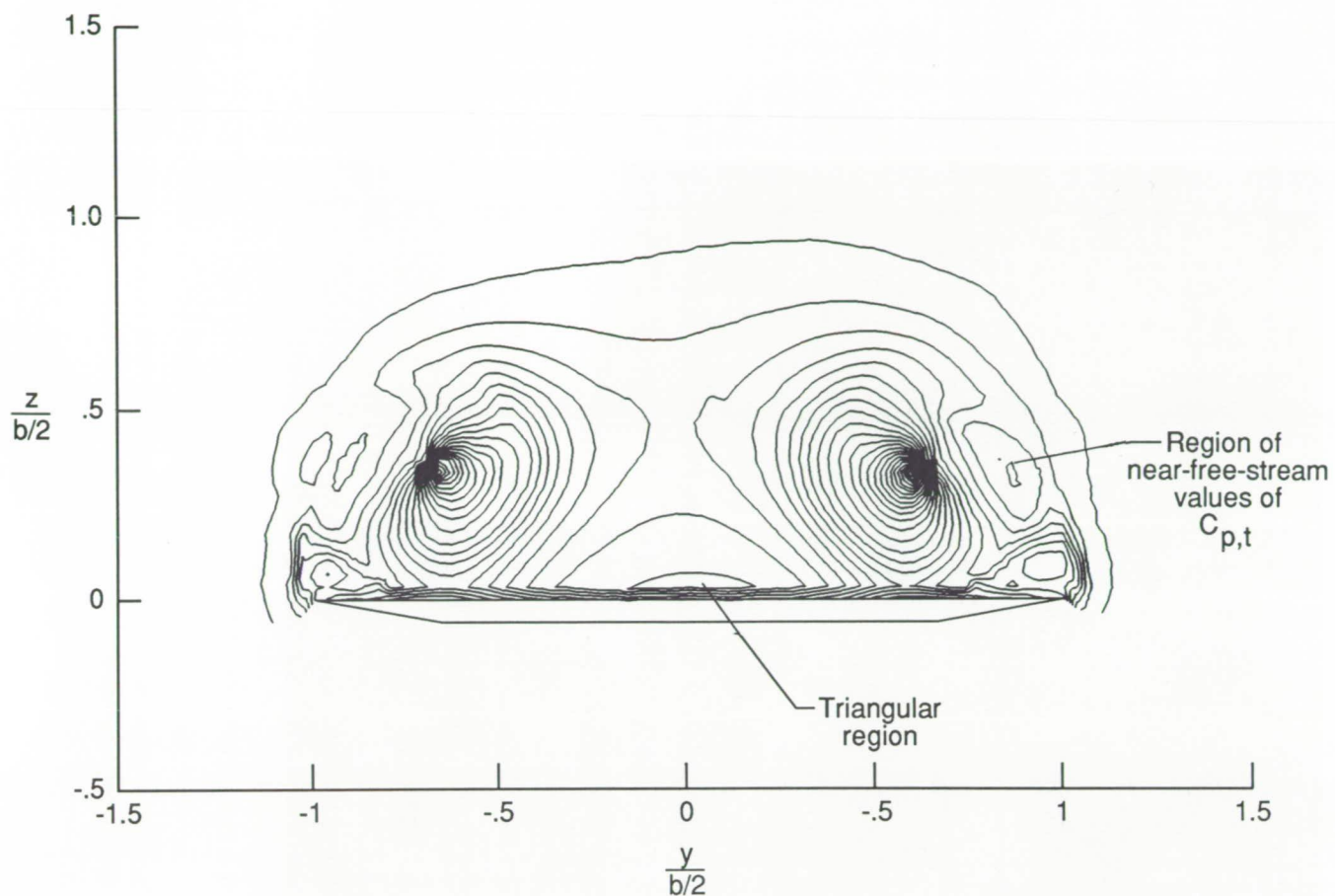
Figure 14. Typical pitot pressure coefficient contours. $x/l = 0.7$; $R = 1.0 \times 10^6$.
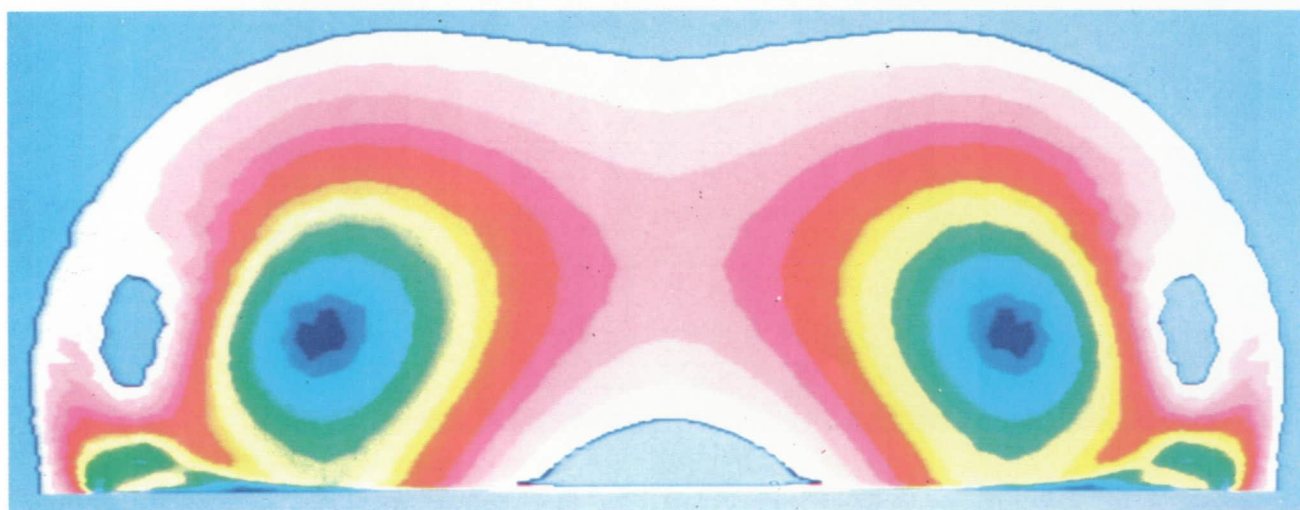
Figure 15. Reduced total pressure coefficient calculated from results of CFL3D Navier-Stokes code. $R = 0.9 \times 10^6$; $x/l = 0.70$.
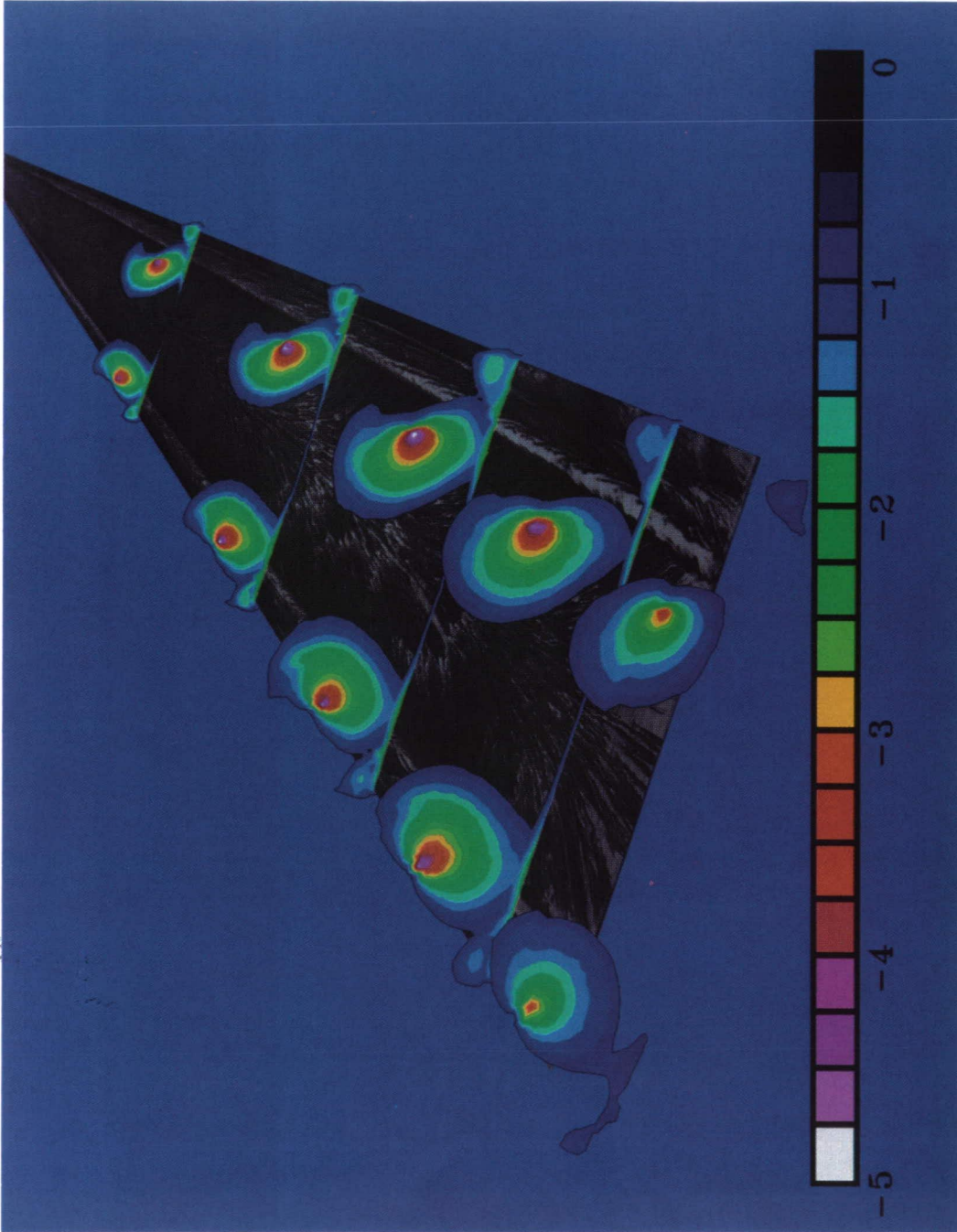
(a) $R = 0.5 \times 10^6$.

Figure 16. Color contours of pitot pressure coefficient superimposed over surface flow visualization.

22
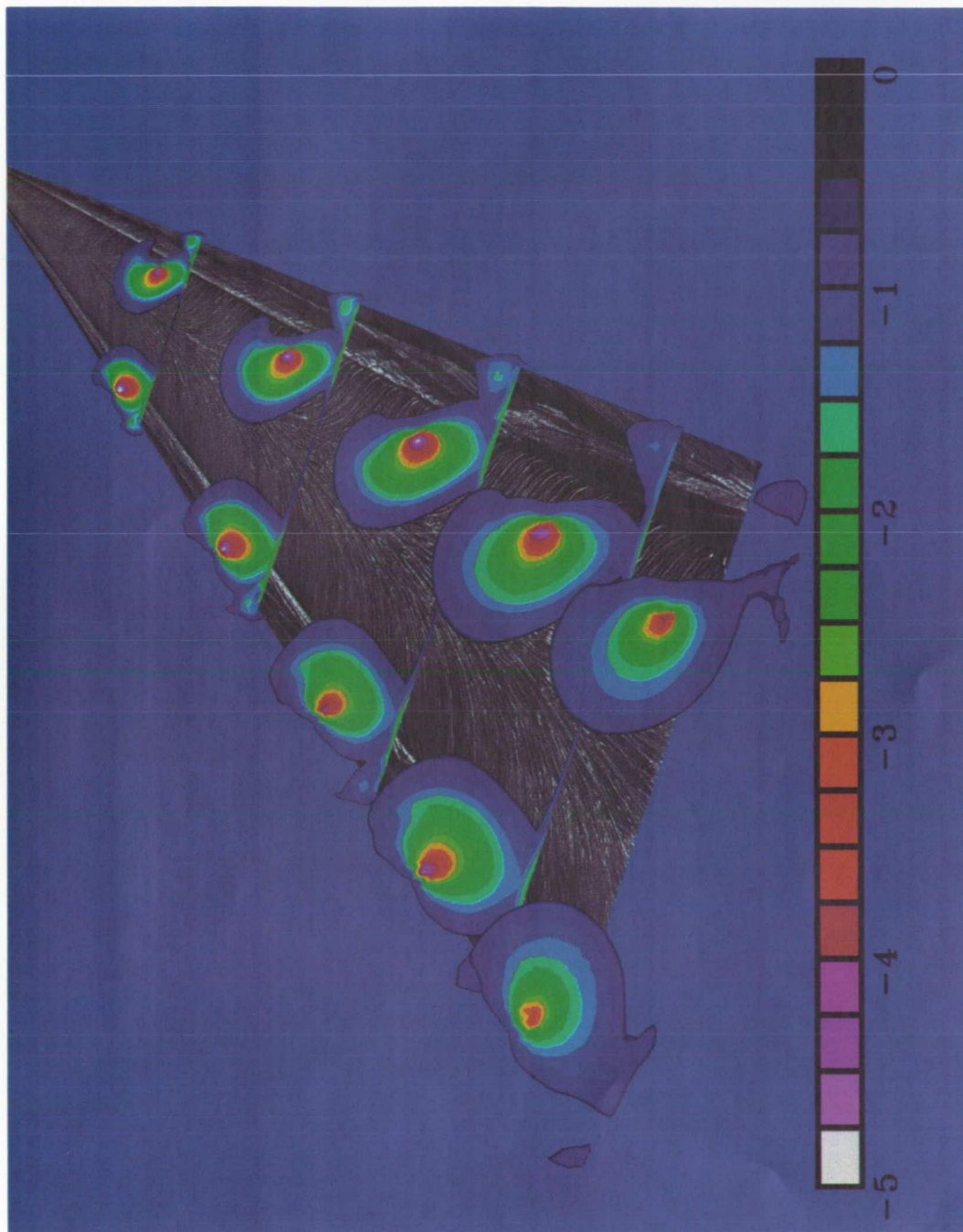
(b) $R = 1.0 \times 10^6$.

Figure 16. Continued.

23
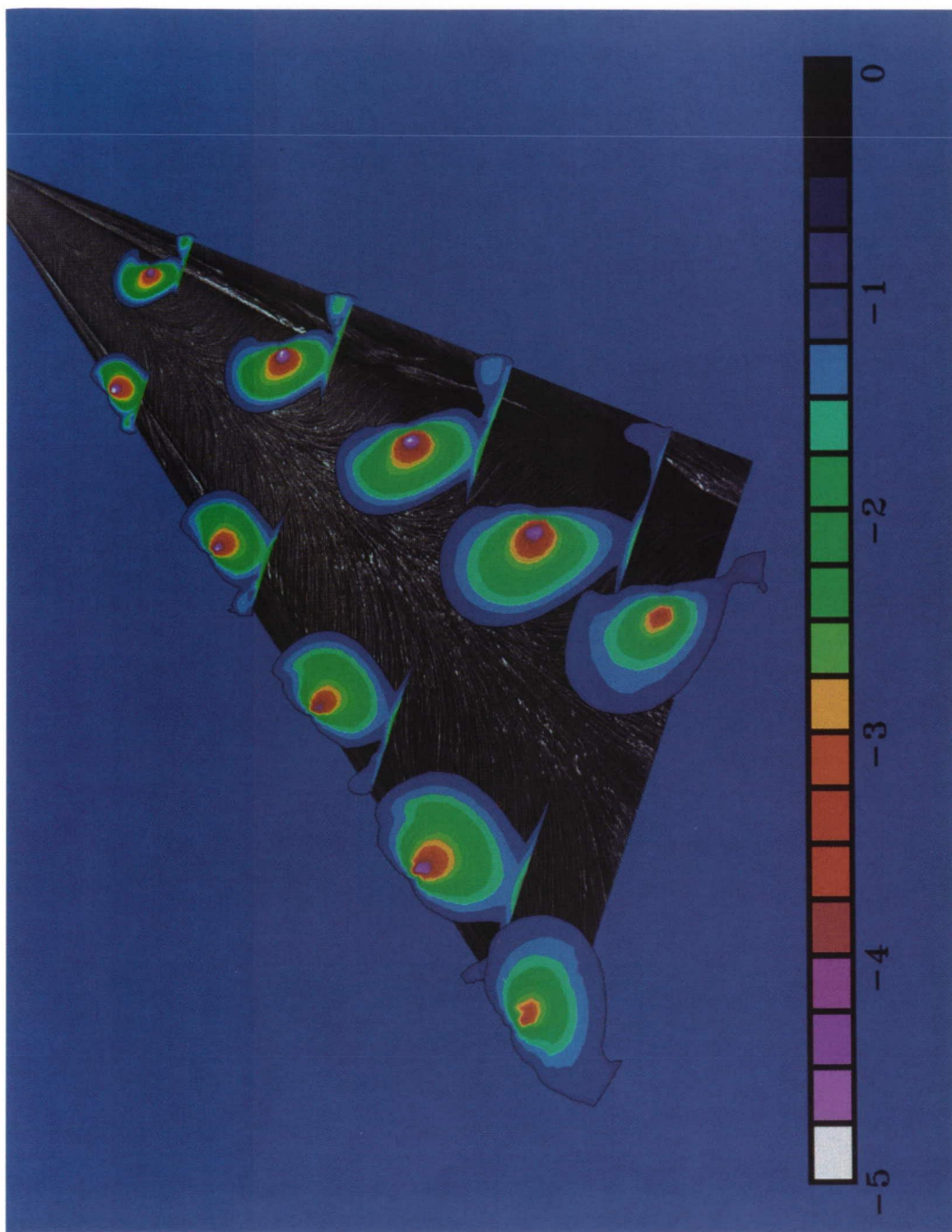
(c) $R = 1.5 \times 10^6$.

Figure 16. Concluded.
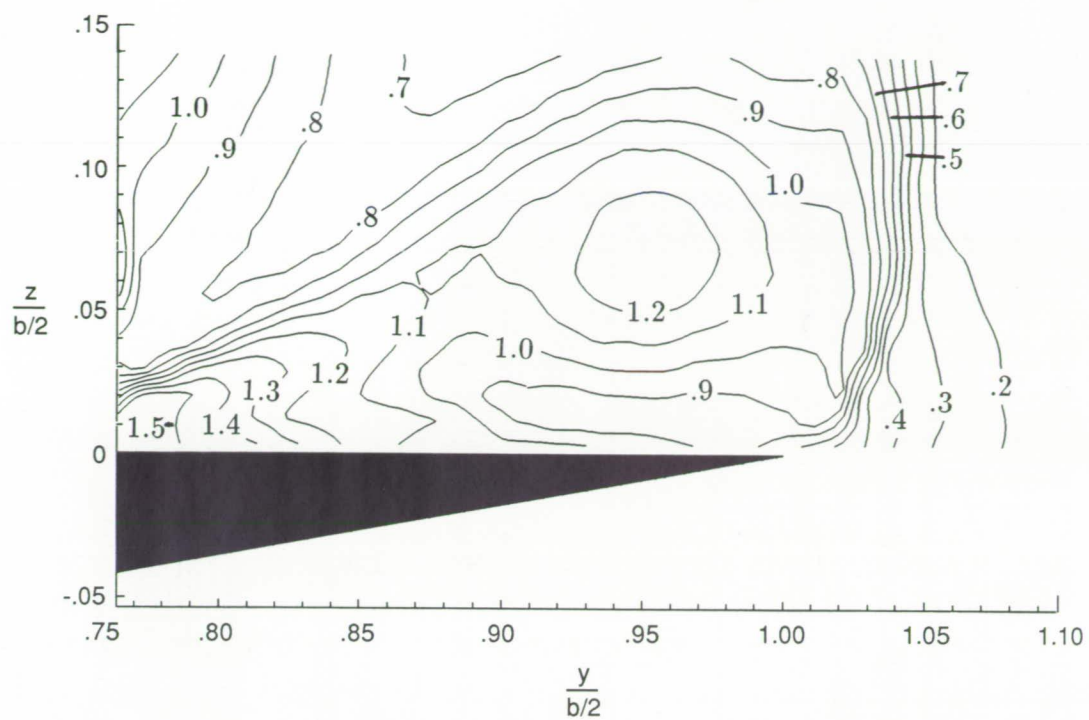
(a) $R = 0.5 \times 10^6$.
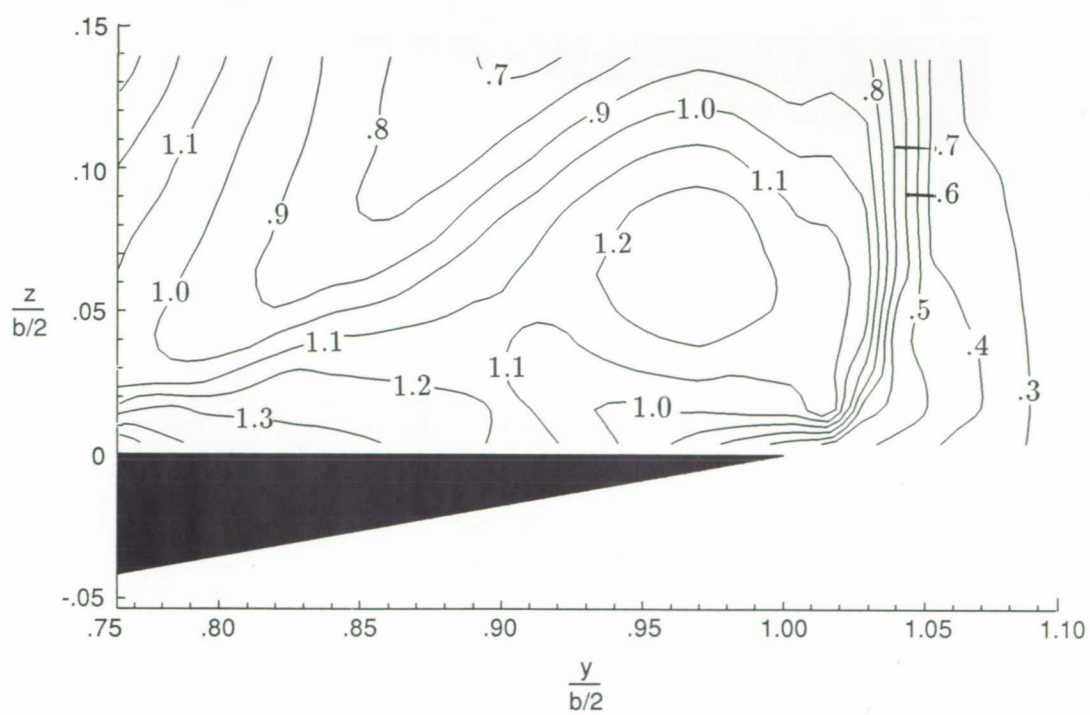
(b) $R = 1.0 \times 10^6$.

Figure 17. Pitot pressure coefficient contours of secondary vortex for $x/l = 0.9$.
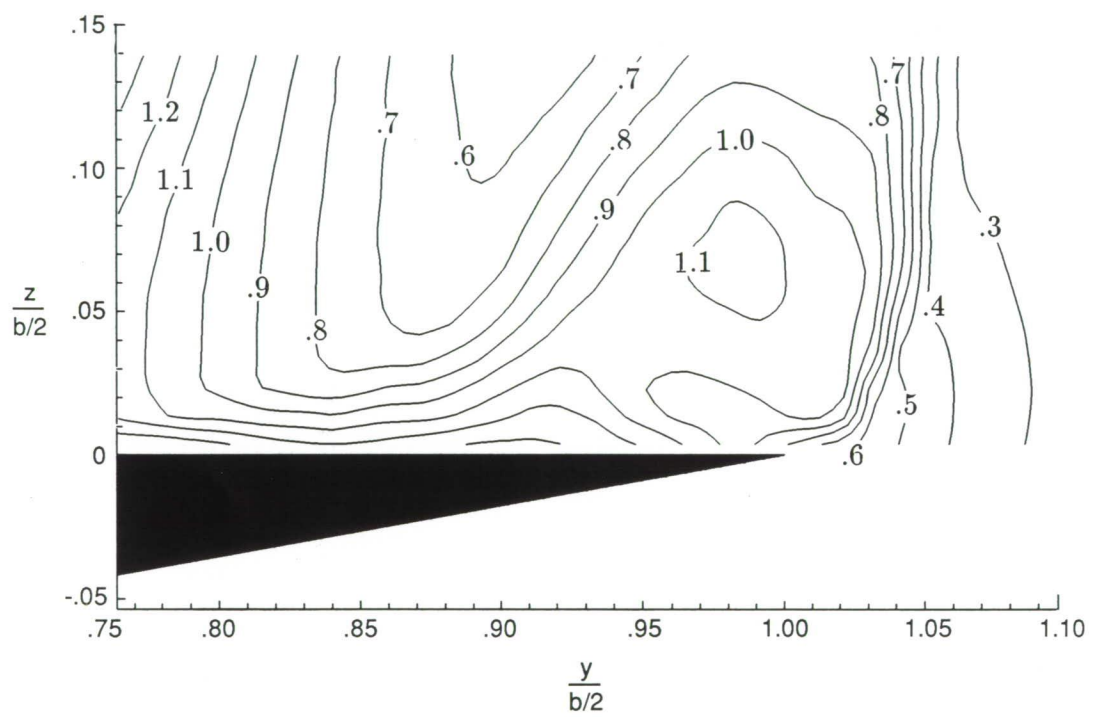
(c) $R = 1.5 \times 10^6$.

Figure 17. Concluded.
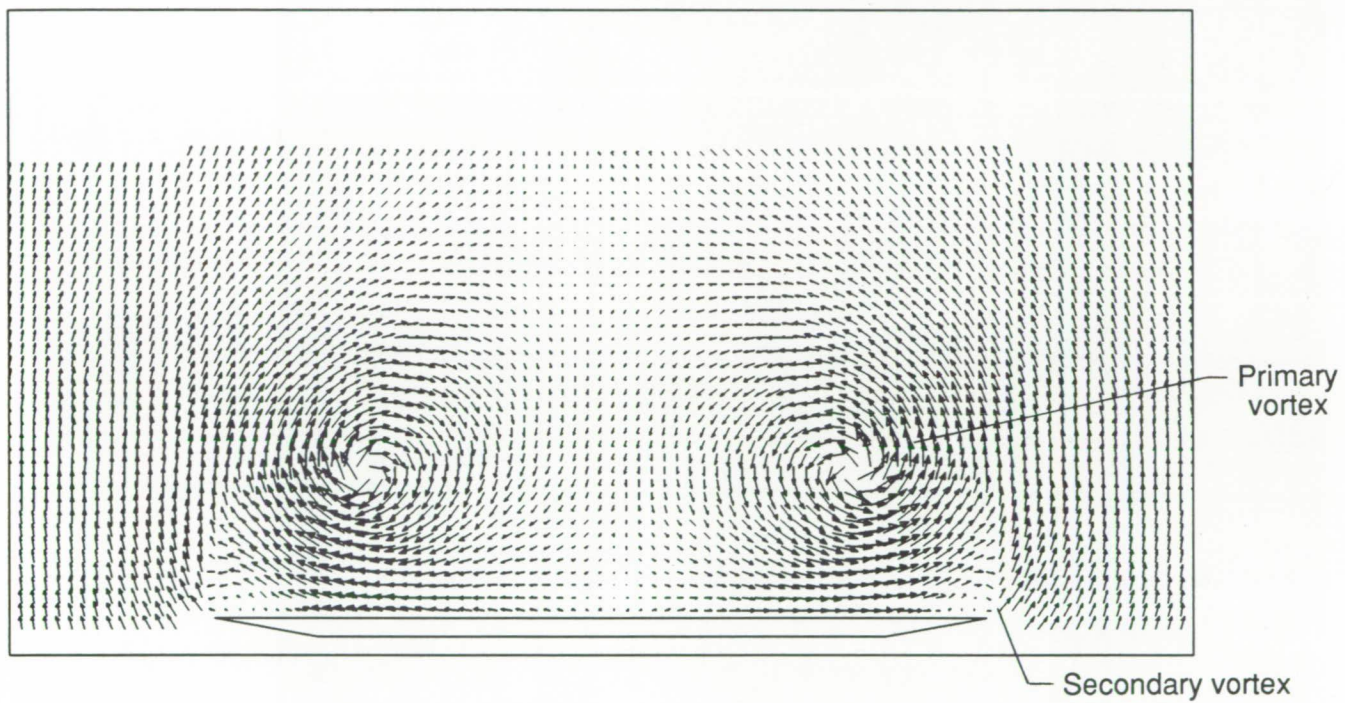
Figure 18. Spatial resolution of typical five-hole probe survey. 93 points horizontally × 36 points vertically.
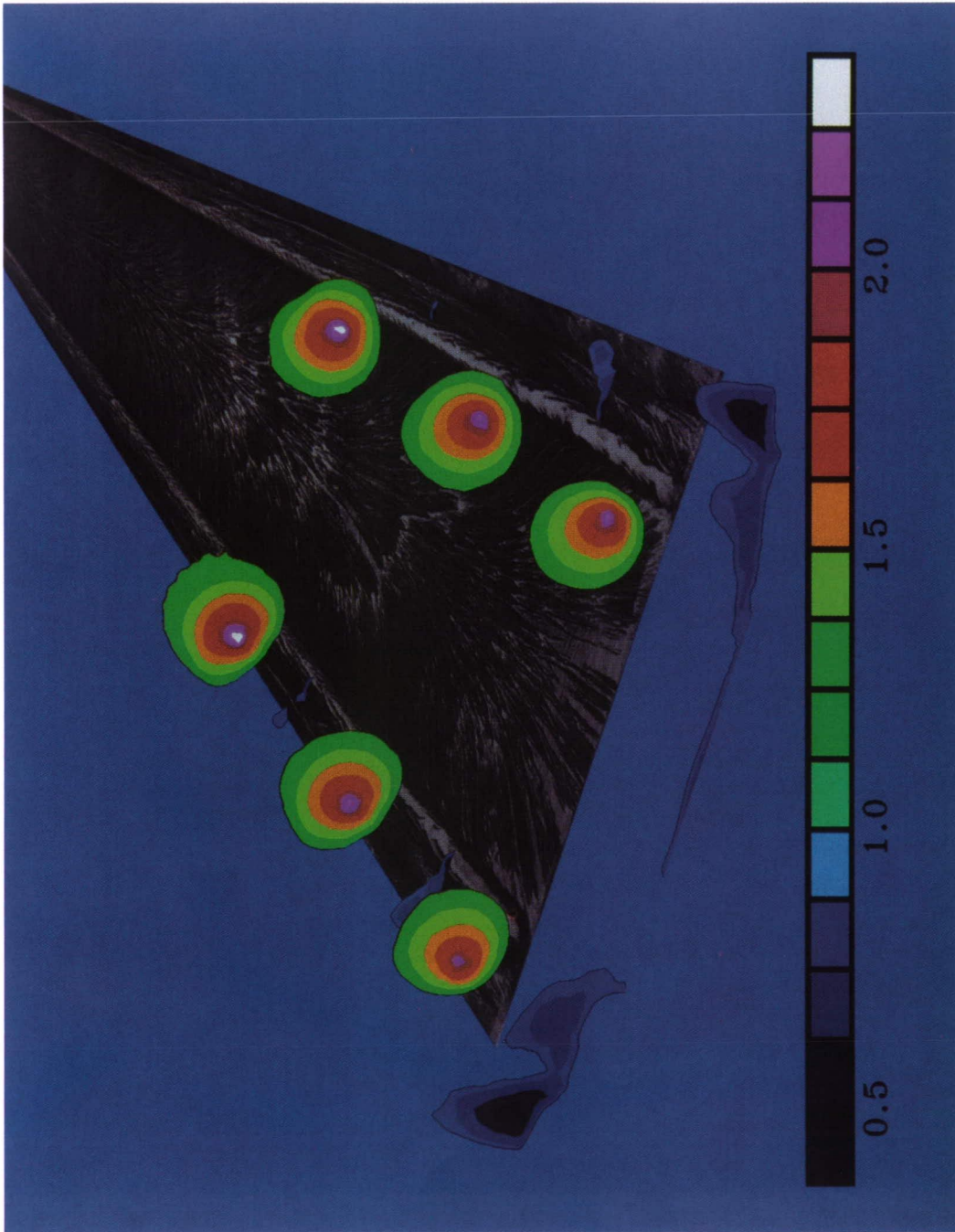
Figure 19. Color contours of nondimensionalized velocity superimposed over surface flow visualization for $R = 0.5 \times 10^6$.
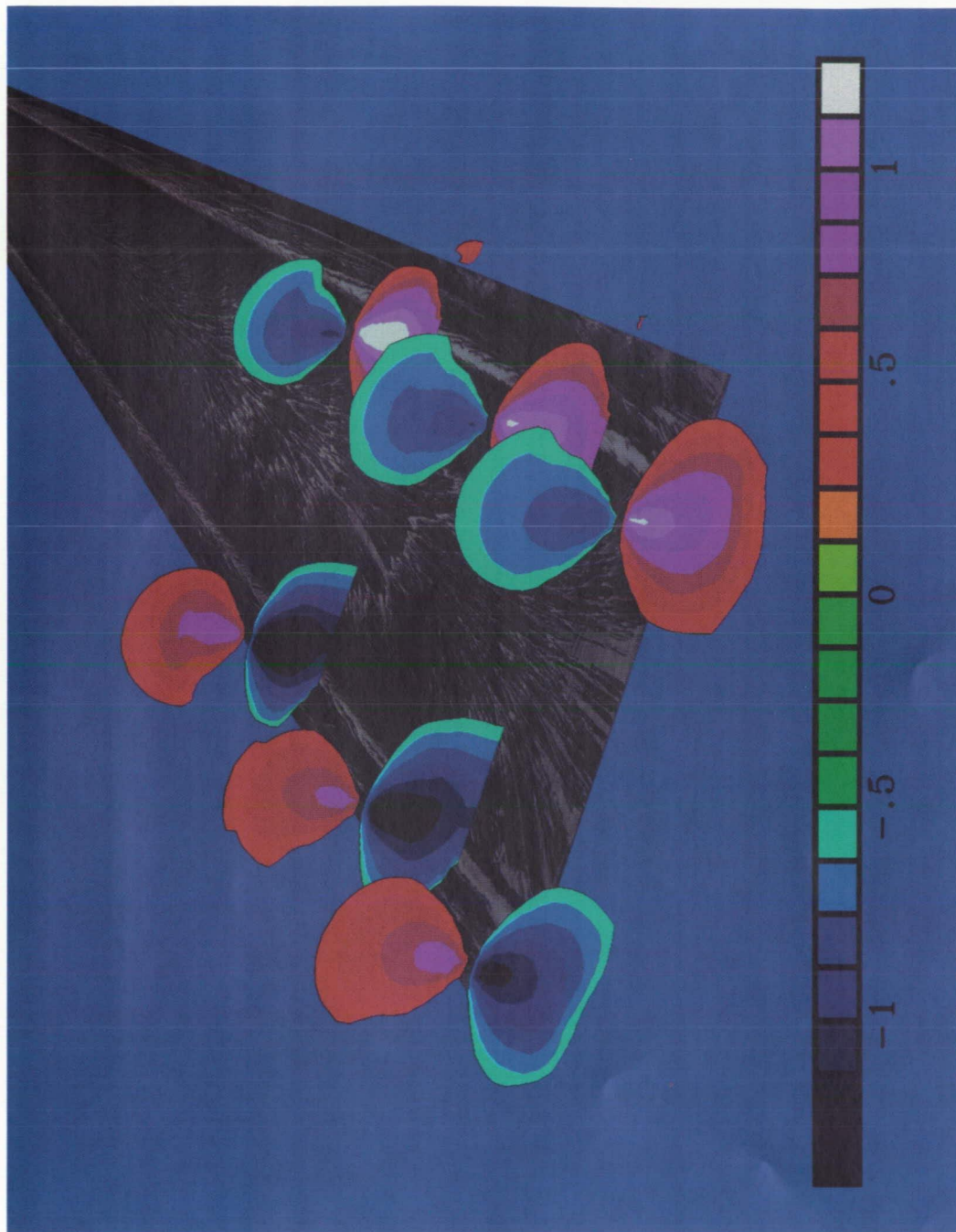
(a) u/U_∞.

(b) v/U_∞.

Figure 19. Continued.

(c) w/U_∞.
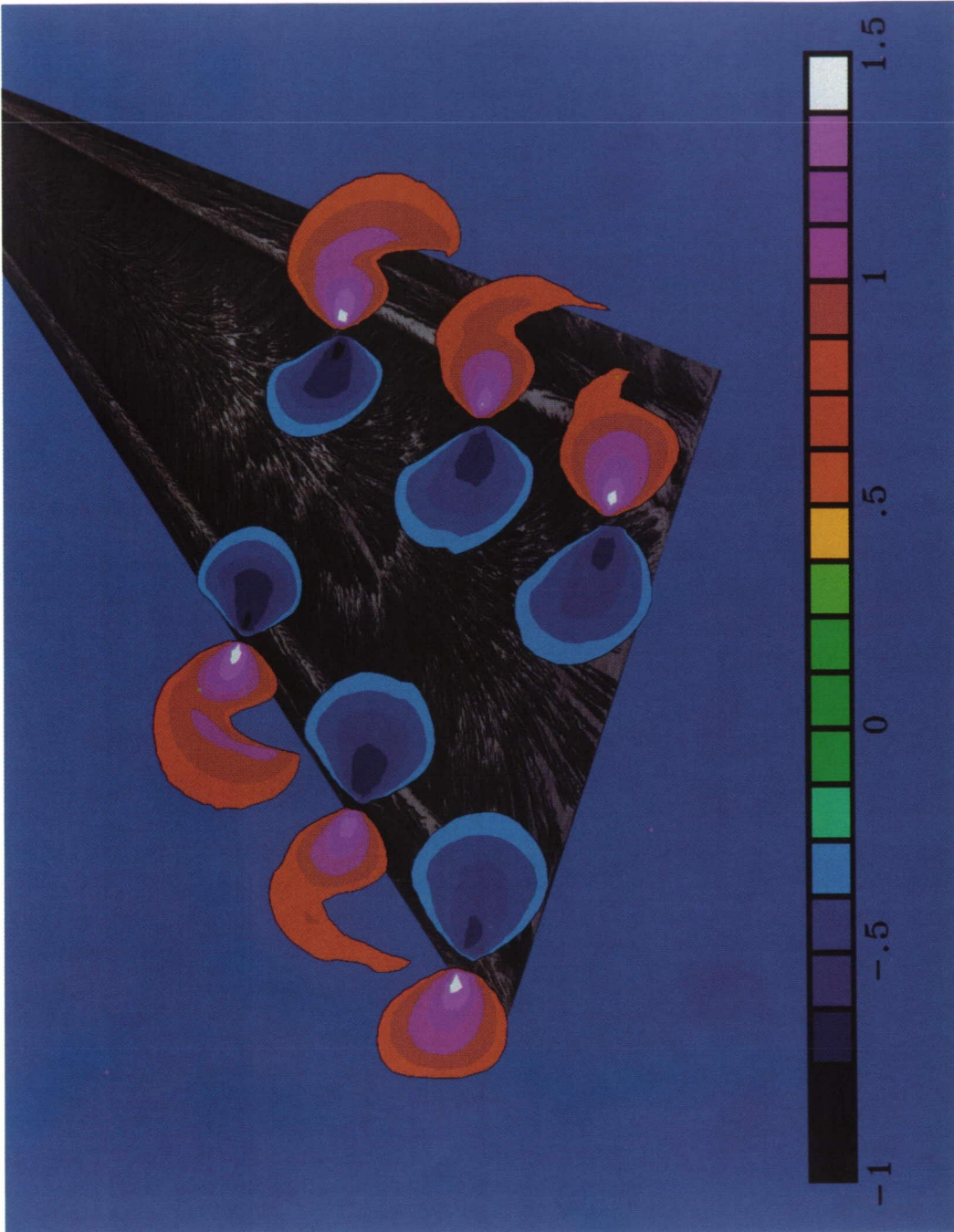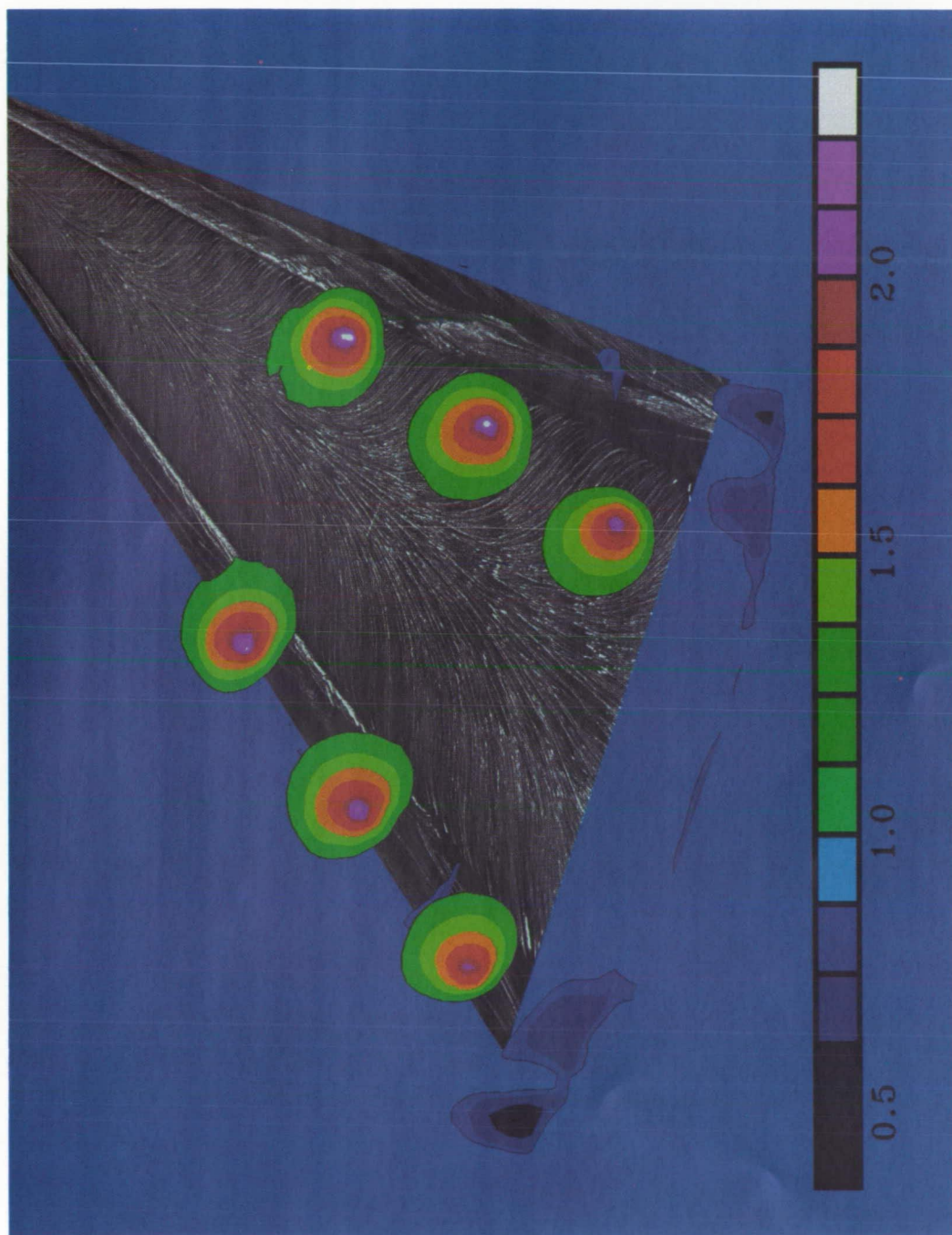
Figure 19. Concluded.

Figure 20. Color contours of nondimensionalized velocity superimposed over surface flow visualization for $R = 1.0 \times 10^6$.
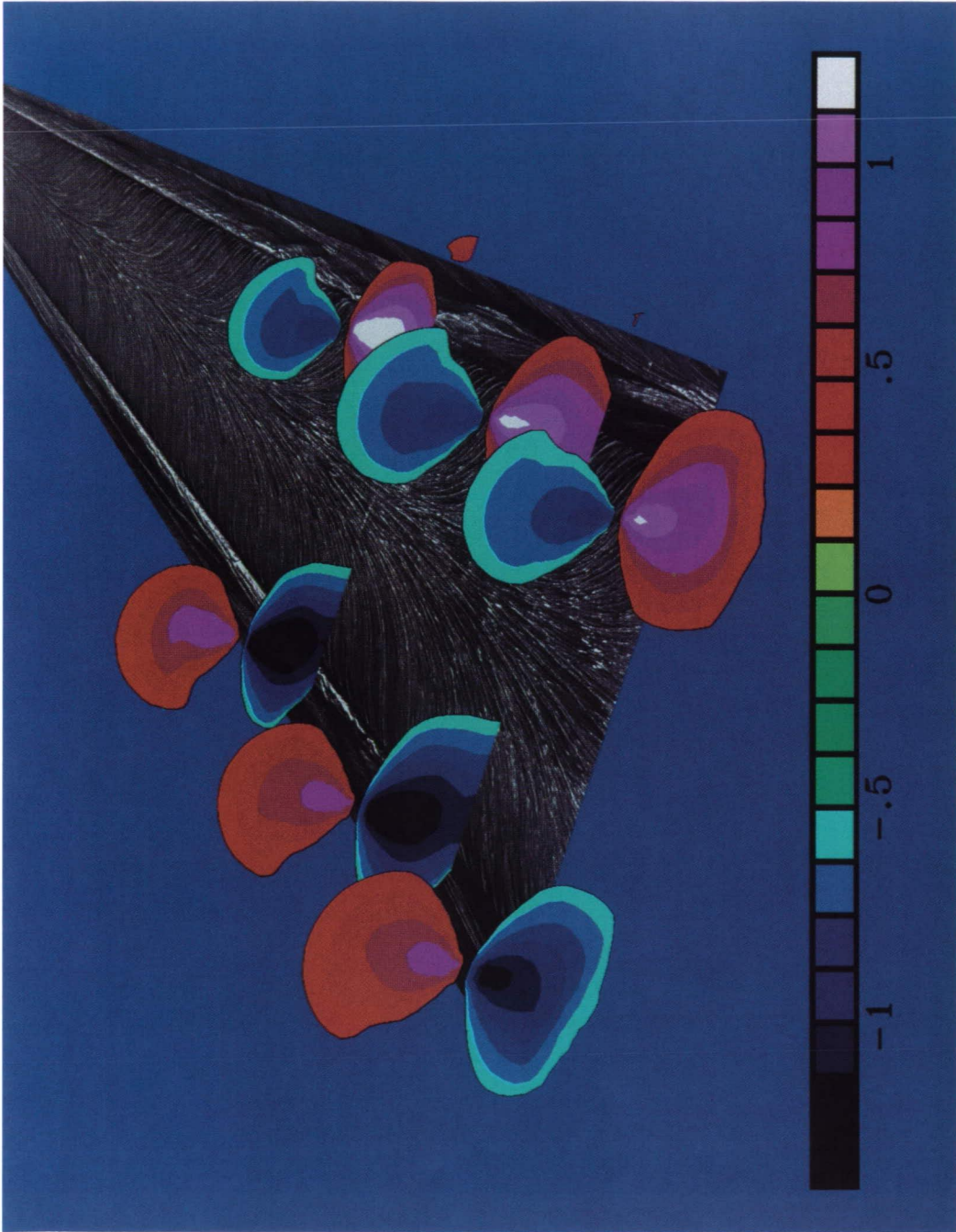
(a) u/U_∞.

31

(b) v/U_∞.

Figure 20. Continued.

32

(c) w/U_∞.
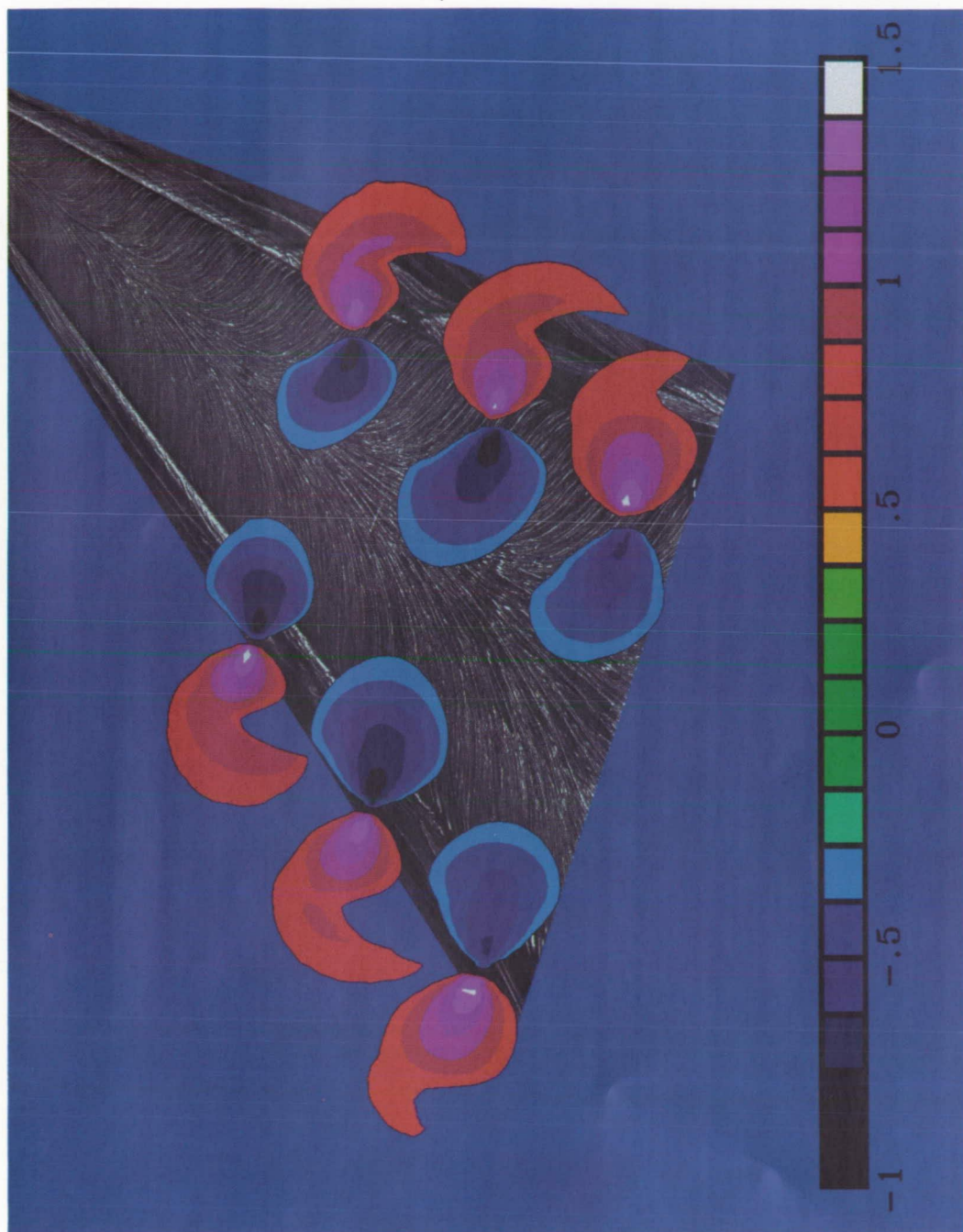
Figure 20. Concluded.
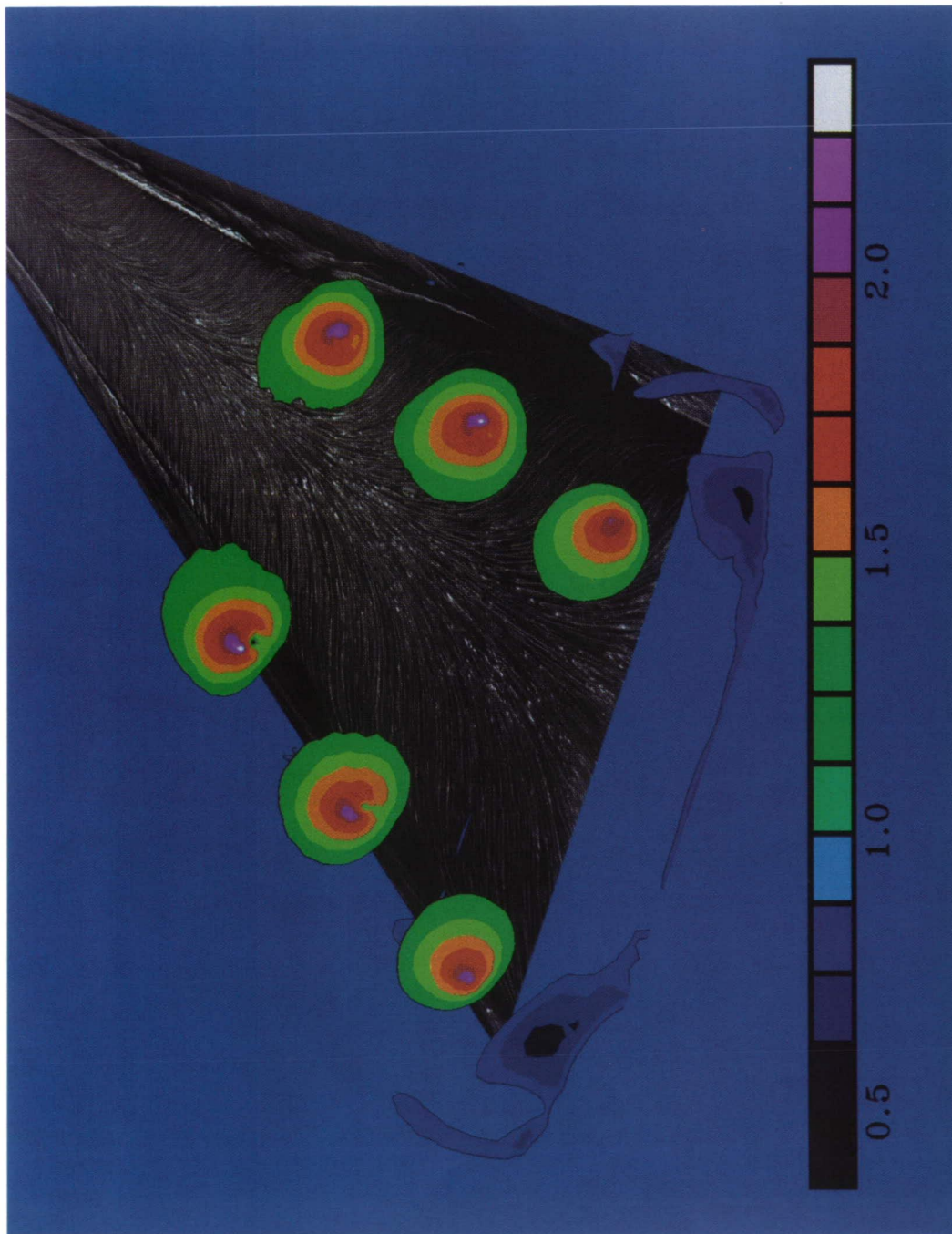
(a) u/U_∞.

Figure 21. Color contours of nondimensionalized velocity superimposed over surface flow visualization for $R = 1.5 \times 10^6$.
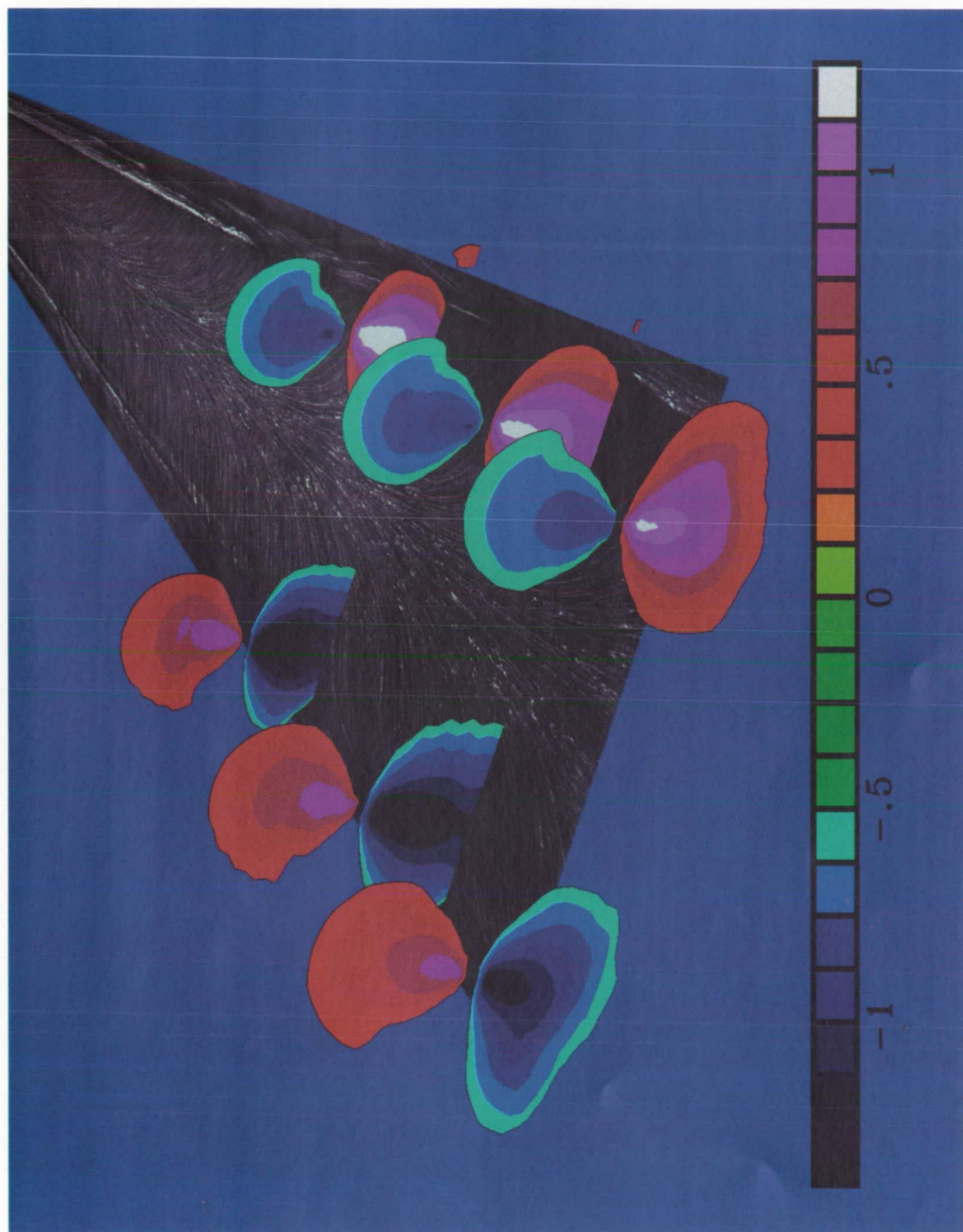
(b) ν/U_∞.

Figure 21. Continued.

(c) w/U_∞.

Figure 21. Concluded.

36
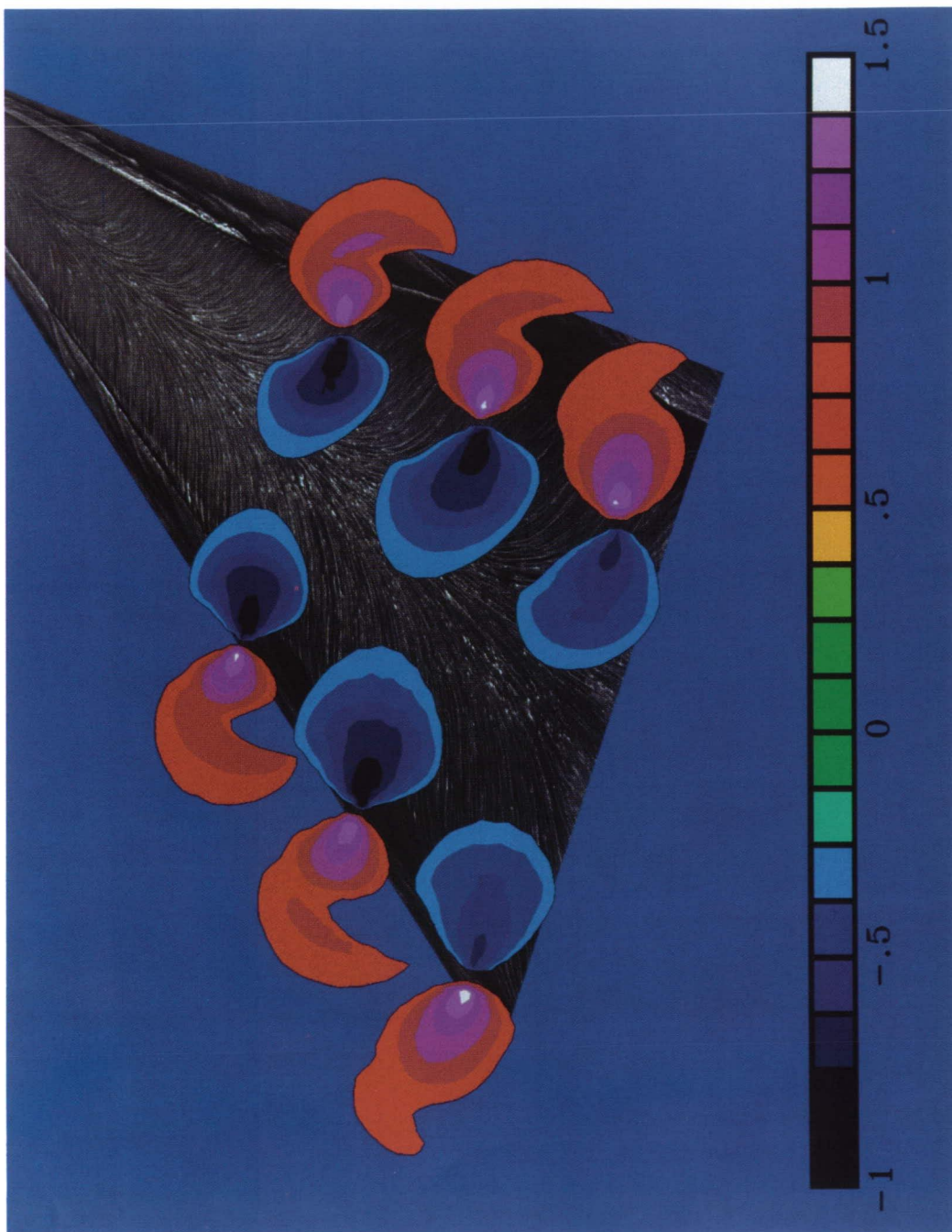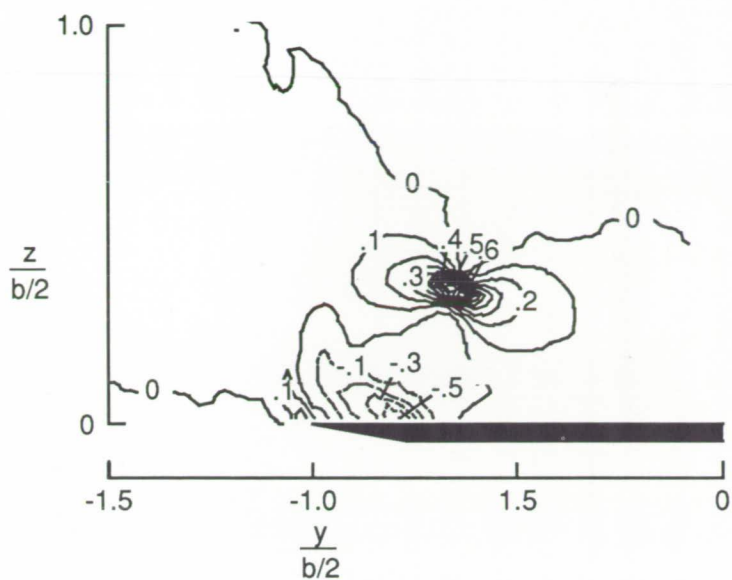
(a) Gradient of lateral component of velocity nondimensionalized by maximum of 6111 $\frac{ft/sec}{ft}$.
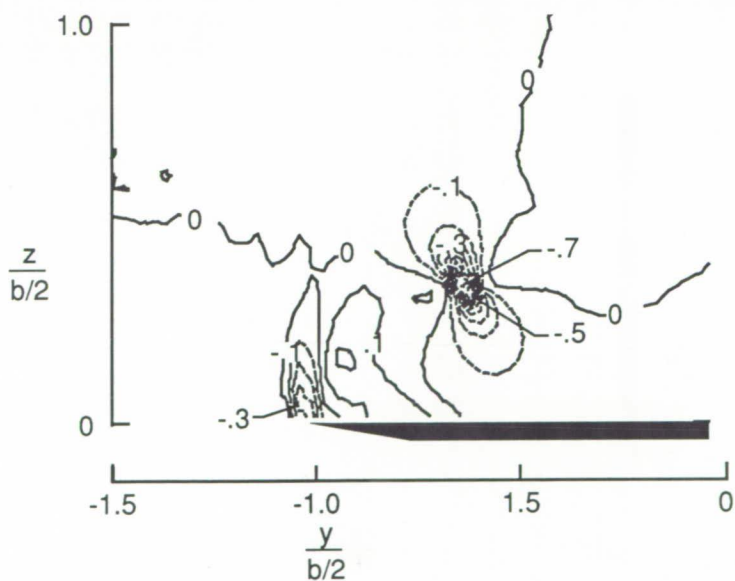
(b) Gradient of vertical component of velocity nondimensionalized by maximum of 7074 $\frac{ft/sec}{ft}$.

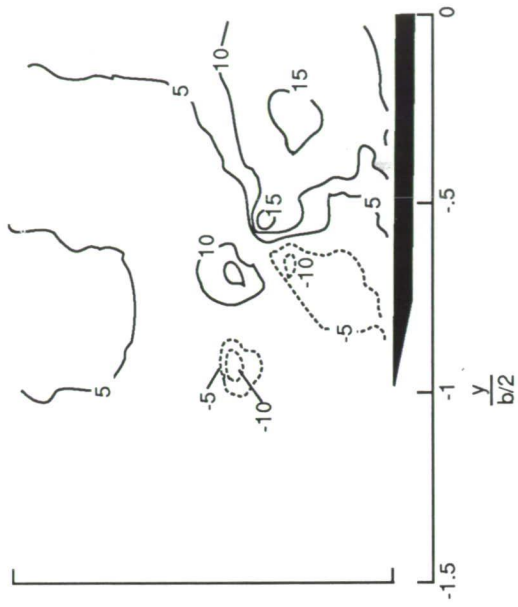Figure 22. Velocity gradients calculated from five-hole probe data. $x/l = 0.9$; $R = 1.0 \times 10^6$.
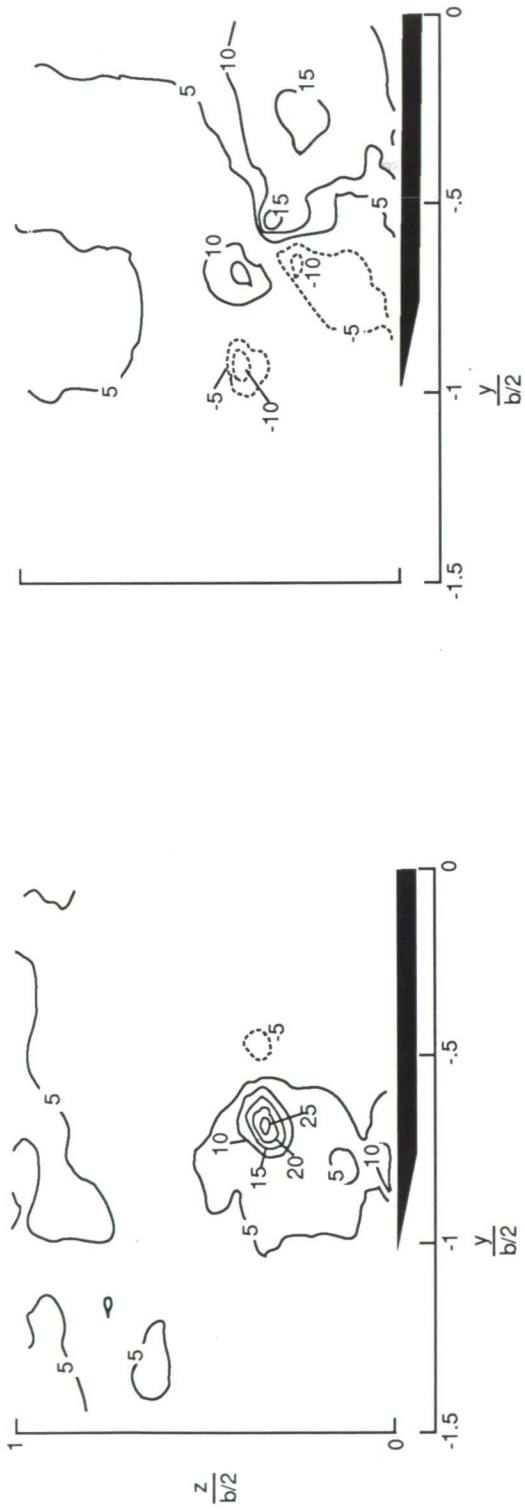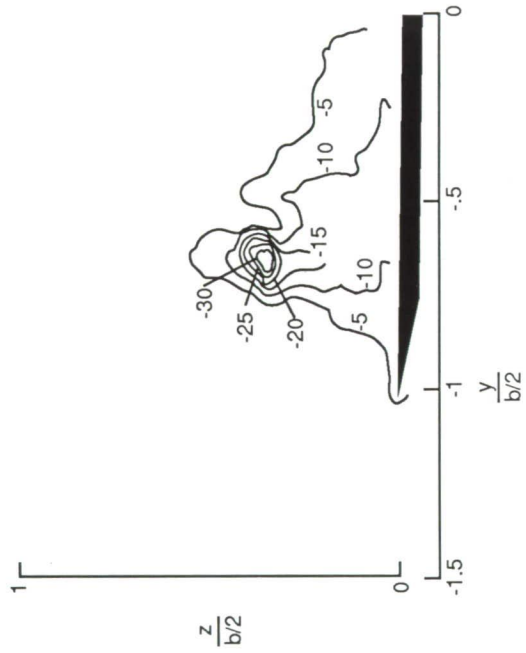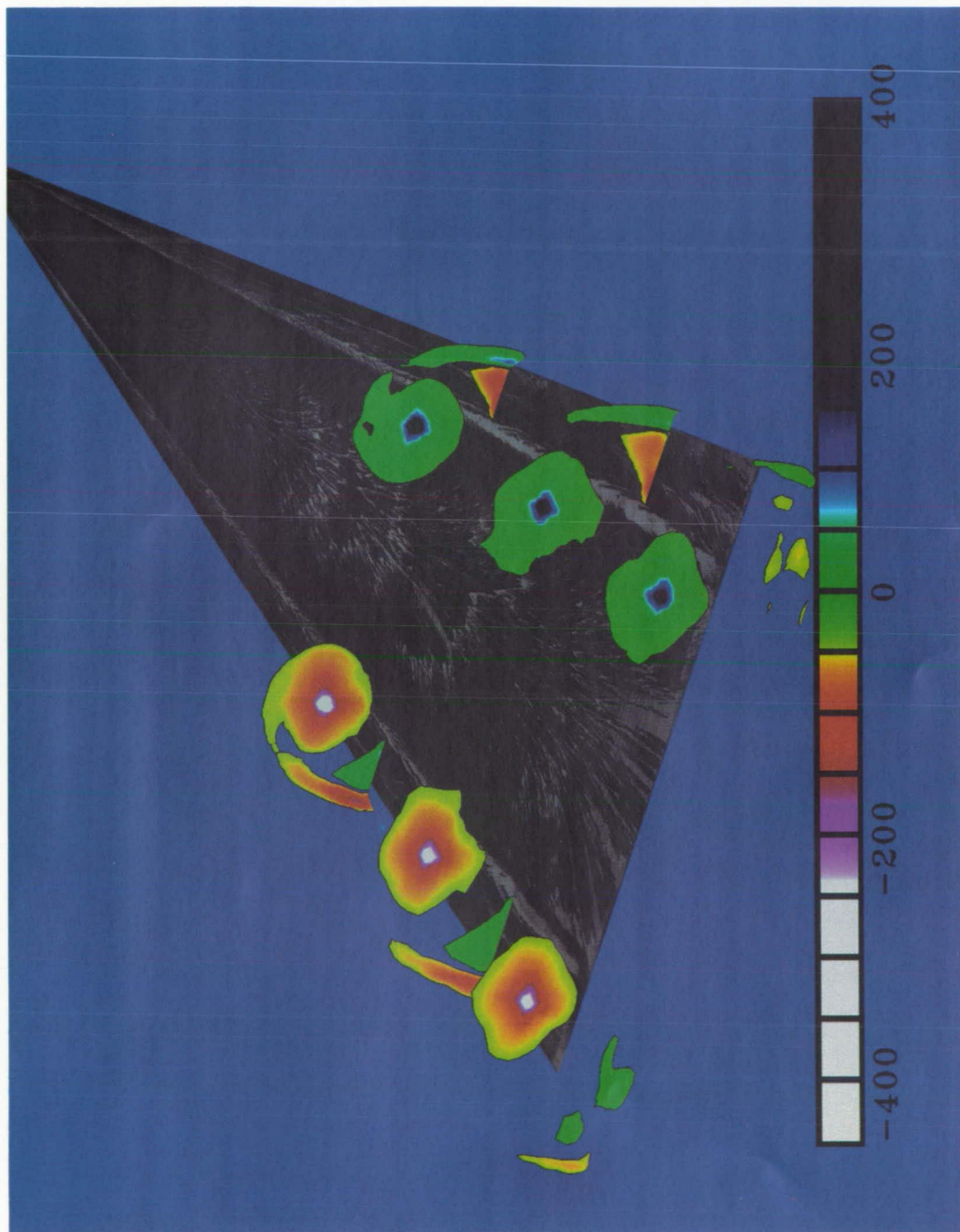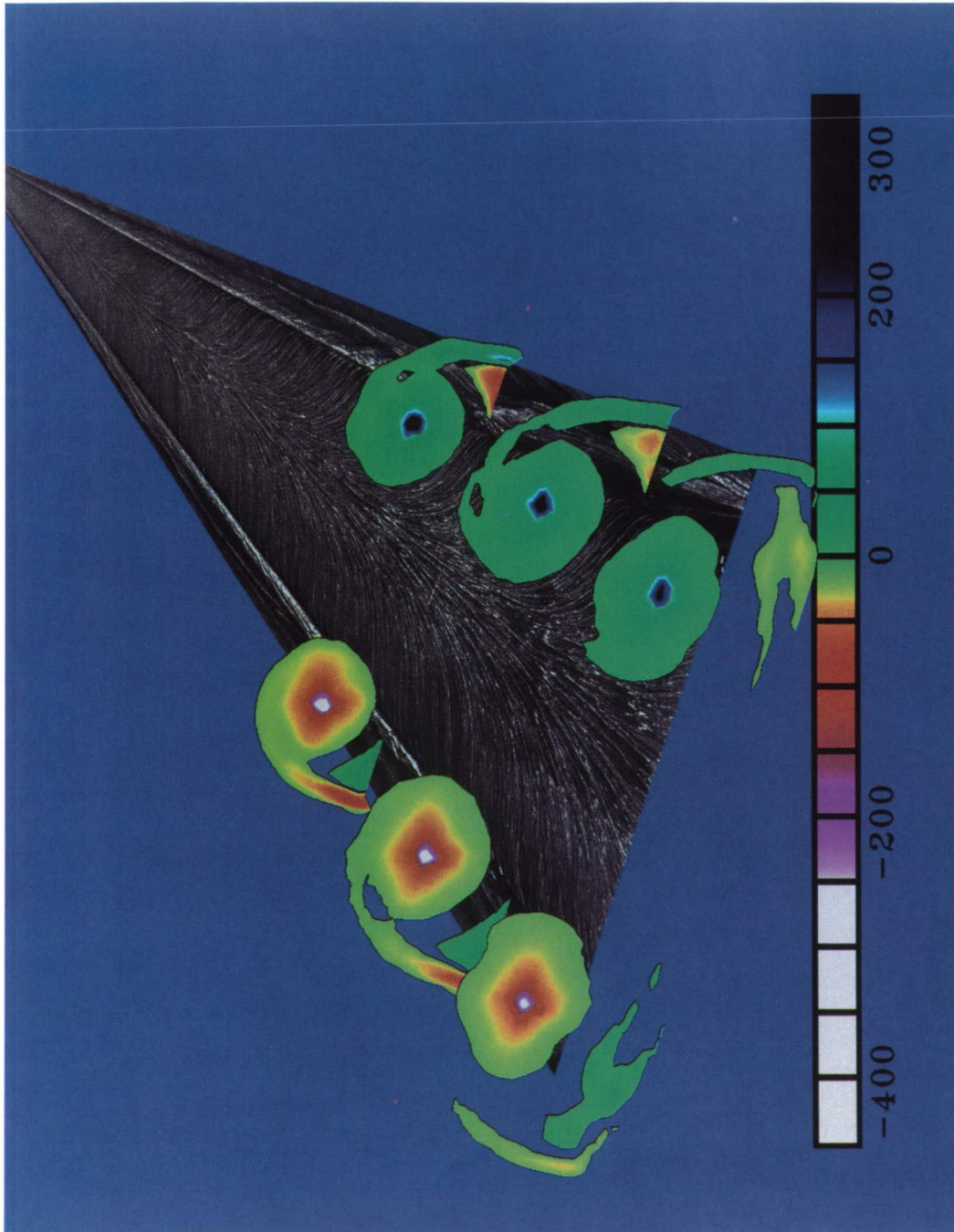
(a) u component.

(b) v component.

(c) w component.

Figure 23. Measured velocities between LV and five-hole probe as percentage of total velocity. $x/l = 0.9$; $R = 1.0 \times 10^6$.
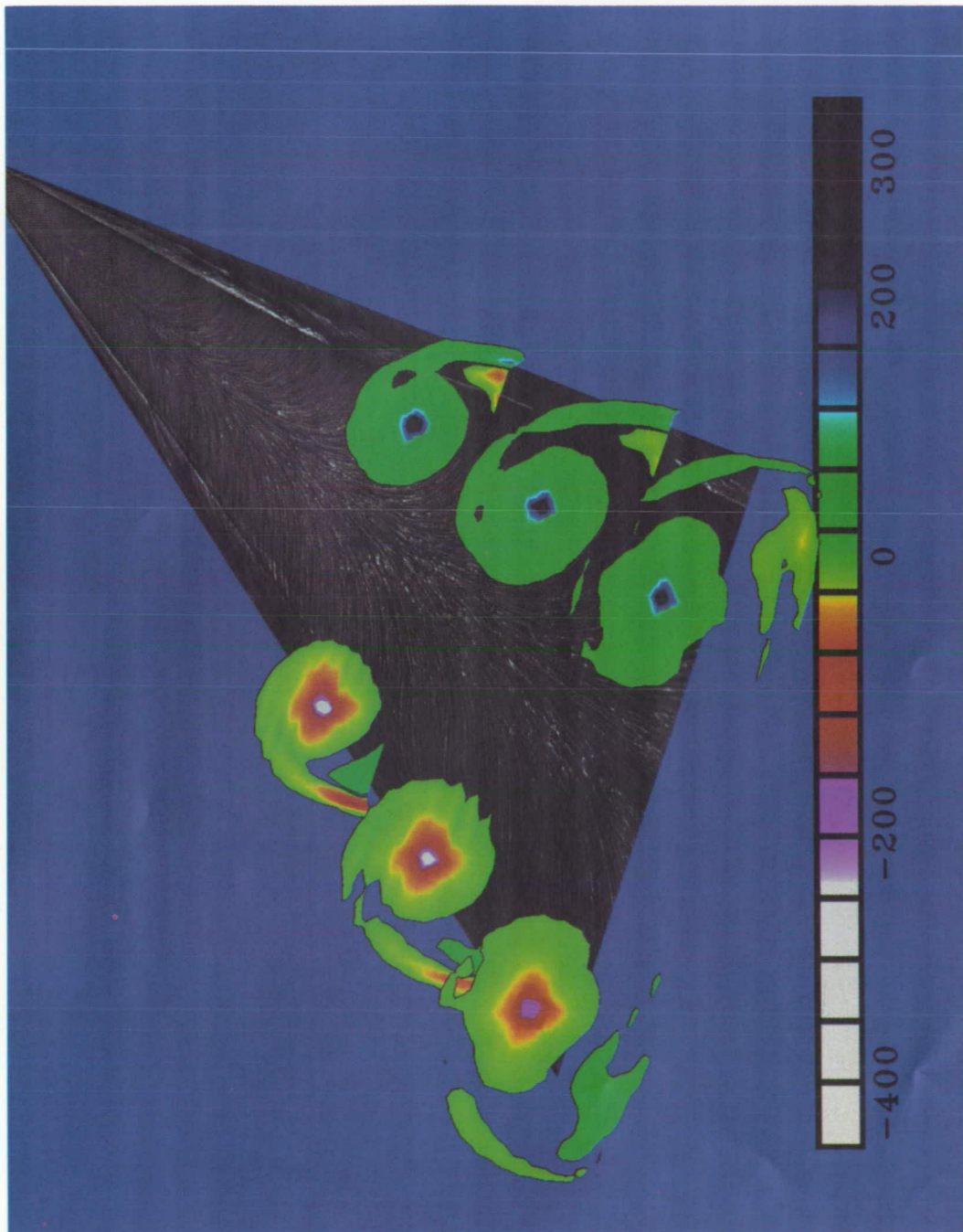
(a) $R = 0.5 \times 10^6$.

Figure 24. Color contours of nondimensionalized vorticity superimposed over surface flow visualization.

39

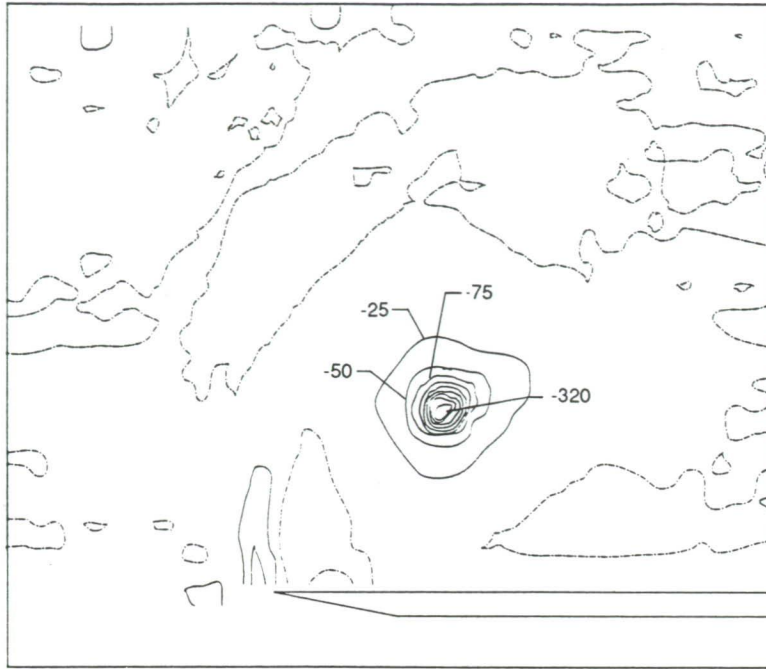(b) $R = 1.0 \times 10^6$.

Figure 24. Continued.

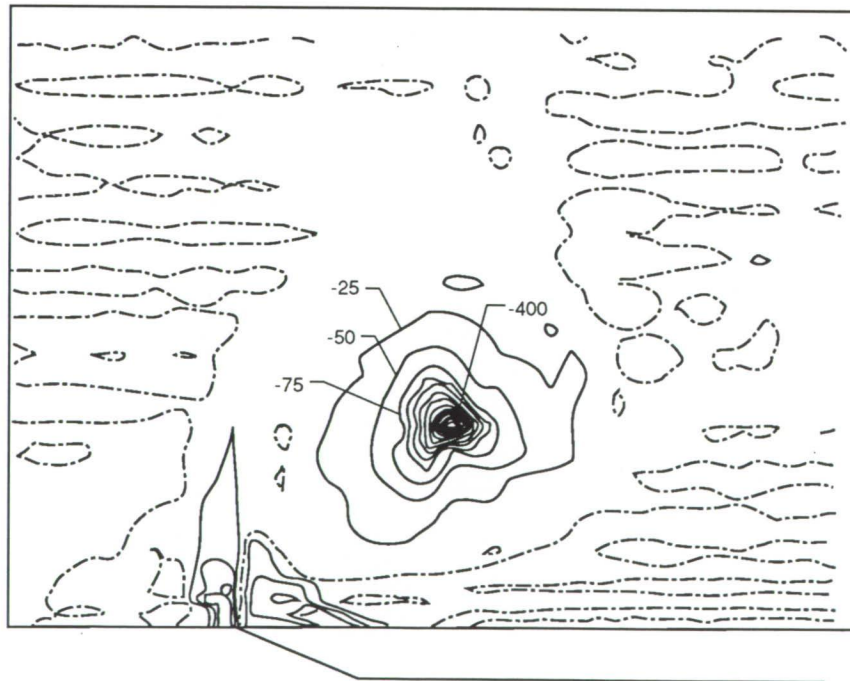(c) $R = 1.5 \times 10^6$.
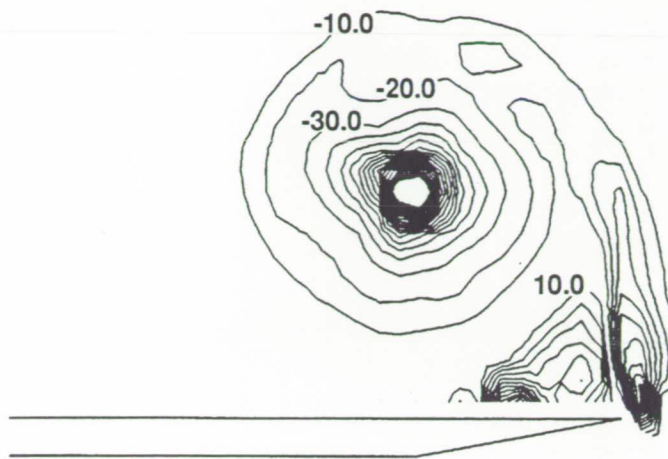
Figure 24. Concluded.

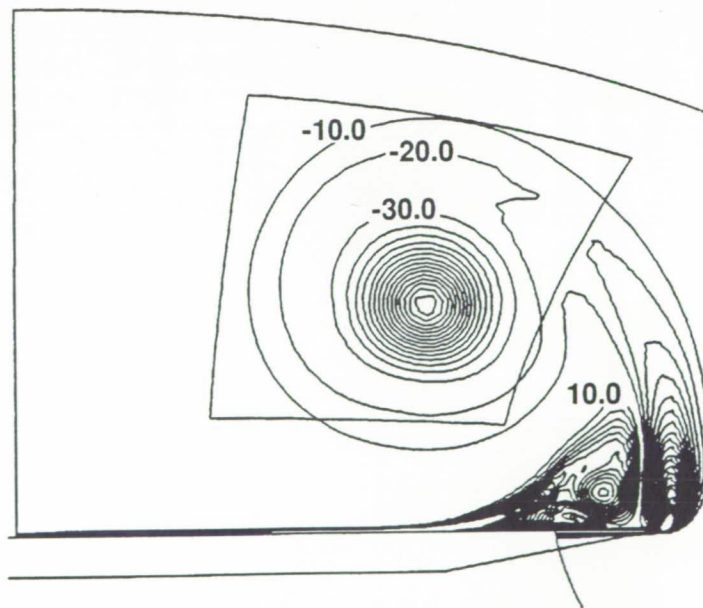(a) Present investigation; $x/l = 0.9$; $R = 1.5 \times 10^6$.

(b) Reference 14; $x/l = 0.8$; $R = 4.0 \times 10^6$.

Figure 25. Calculated vorticity from present investigation and reference 14.

(a) Experiment.

(b) Computation (ref. 15).

Figure 26. Experimental and computational vorticity. $R = 0.5 \times 10^6$; $x/l = 0.7$:

NASA National Aeronautics and Space Administration	Report Documentation Page	

1. Report No. NASA TP-2997	2. Government Accession No.	3. Recipient's Catalog No.
4. Title and Subtitle Detailed Flow-Field Measurements Over a 75° Swept Delta Wing		5. Report Date October 1990
		6. Performing Organization Code
7. Author(s) Scott O. Kjelgaard and William L. Sellers III		8. Performing Organization Report No. L-16718
9. Performing Organization Name and Address NASA Langley Research Center Hampton, VA 23665-5225		10. Work Unit No. 505-60-11-03
		11. Contract or Grant No.
12. Sponsoring Agency Name and Address National Aeronautics and Space Administration Washington, DC 20546-0001		13. Type of Report and Period Covered Technical Paper
		14. Sponsoring Agency Code

15. Supplementary Notes

16. Abstract

Results from an experimental investigation documenting the flow field over a 75° swept delta wing at an angle of attack of 20.5° are presented. Results obtained in the investigation include surface flow visualization, off-body flow visualization, and detailed flow-field surveys. Flow-field surveys at Reynolds numbers of 0.5×10^6, 1.0×10^6, and 1.5×10^6 based on the root chord were conducted with both a pitot pressure probe and a five-hole pressure probe. Three-component laser velocimeter surveys were conducted at a Reynolds number of 1.0×10^6. The pitot pressure surveys were obtained at five chordwise stations, the five-hole probe surveys were obtained at three chordwise stations, and the laser velocimeter surveys were obtained at one station. The velocity measurements indicate that Reynolds number has little effect on the global structure of the flow field for the test Reynolds number range. Measurements of the nondimensionalized axial velocity in the core of the vortex indicate a jet-like flow with values greater than twice free stream. Comparisons between velocity measurements from the five-hole pressure probe and the laser velocimeter indicate that the pressure probe does a reasonable job of measuring the flow-field quantities where the velocity gradients in the flow field are low.

17. Key Words (Suggested by Authors(s)) Vortex flow Delta wing Velocity measurement Laser velocimetry Five-hole probe Flow visualization	18. Distribution Statement Unclassified—Unlimited Subject Category 02	
19. Security Classif. (of this report) Unclassified	20. Security Classif. (of this page) Unclassified	21. No. of Pages 44 22. Price A03

NASA FORM 1626 OCT 86

NASA-Langley, 1990